# An Efficient Finite Shell Element for the Static Response of Piezoelectric Laminates

**— Source link** ⤴

Philippe Vidal, Michele D'Ottavio, Mehdi Ben Thaïer, Olivier Polit

**Institutions:** University of Paris

Related papers:

- Advances in piezoelectric finite element modeling of adaptive structural elements: a survey

- Mechanics of laminated composite plates and shells : theory and analysis

- A refined sinus finite element model for the analysis of piezoelectric-laminated beams

- Use of piezoelectric actuators as elements of intelligent structures

- An efficient standard plate theory

# An efficient finite shell element for the static response of piezoelectric laminates

P. Vidal, M. d'Ottavio, M. Ben Thaïer, O. Polit

# An Efficient Finite Shell Element for the Static Response of Piezoelectric Laminates

PHILIPPE VIDAL,* MICHELE D'OTTAVIO, MEHDI BEN THAÏER AND OLIVIER POLIT

*Laboratoire d'Energétique, Mécanique et Electromagnétisme, Université Paris Ouest Nanterre La Défense, 50 rue de Sèvres, 92410 Ville d'Avray, France*

**ABSTRACT:** This study presents a novel finite element (FE) for shell structures including piezoelectric actuators and sensors. Based on a conventional 8-node shell formulation and the classical displacement-based variational formulation, the present element has an enriched description of the transverse kinematics in order to consistently retain the full three-dimensional (3D) piezoelectric coupling. Furthermore, a layer-wise description of the electric degrees of freedom permits to account for embedded piezoelectric actuators and sensors. The robustness of the FE is enhanced by referring to an established technique that avoids transverse shear locking and membrane locking. Numerical results are given which validate the present implementation and highlight the efficiency and accuracy of the proposed formulation. Additionally, some new reference solutions for the static behavior of piezoelectric shells are provided by means of 3D FE computations with a commercial software.

*Key Words:* multilayered shell element, piezoelectric actuators and sensors, refined model, three-dimensional constitutive law, reference solutions.

## INTRODUCTION

IN the last decades, numerous industrial domains are being attracted toward high-performance structures whose functionality is extended beyond the passive load-bearing capability (Gibson, 2010). Structural health monitoring, active vibration damping, and energy harvesting are only some examples of possible applications of a multifunctional structural component. Piezoelectric materials permit to convert mechanical and electrical energy at frequency ranges that are most interesting for technical applications such as vibration damping and rapid shape adaptation (Chopra, 2002). Due to the complex manufacturing of such structural devices, a reliable numerical analysis tool is necessary to capture all the relevant phenomena that guide the design process. Furthermore, if optimization processes and runtime control algorithms are addressed, the numerical simulation tool should be as robust and efficient as possible.

In this framework, several reduced structural models have been proposed which account for the presence of piezoelectric actuators and sensors. The mathematical representation of the piezoelectric coupling must account for the mode of actuation and the electrical boundary conditions (Rogacheva, 1994). Basically, two

actuation modes can be considered in thin shell structure applications the longitudinal extension mode (31-mode), in which the polarization vector and the actuating electric field are parallel and act in the layer's thickness direction, and the shear actuation (15-mode), in which the polarization vector and the actuating electric field are perpendicular (Benjeddou et al., 2000). We shall limit the scope of this contribution to the most common longitudinal extension mode. Thin piezoelectric actuators working in 31-mode can be modeled in a first approximation by assuming a constant electric field along the thickness direction. However, the constant electric field assumption prevents an electric field to be induced by the mechanical deformation, which is the *direct piezoelectric effect* exploited in sensor applications. Note that the induced field increases the apparent stiffness of the plate by means of an additional 'electric stiffness' term. In order to correctly represent this effect, an at least quadratic approximation for the thickness distribution of the electric potential should be employed (Bisegna and Maceri, 1996; D'Ottavio and Polit, 2009).

The inclusion of piezoelectric sensors/actuators in the load path of the host structure naturally leads to a multifunctional composite component. An exhaustive review with assessment of some typical models for piezoelectric laminates has been provided by Saravanos and Heyliger (1999). As pointed out in numerous works, e.g., by Gopinathan et al. (2000); Ballhause et al. (2005); Carrera and Brischetto (2007), the piezoelectric coupling and the presence of electrical and mechanical

interfaces sharpens the limits of classical, low-order reduced models such as Classical Lamination Theory (CLT) and First-order Shear Deformation Theory (FSDT). To accurately capture the local response, a so-called layer-wise description of the laminate is necessary, whose computational cost, however, depends on the number of layers. Equivalent single layer descriptions, in which the number of unknowns is independent of the number of layers, prove useful for a global response analysis (Robbins Jr and Chopra, 2006; Carrera et al., 2007). The possibility to impose independent electrical boundary conditions at each piezoelectric layer in the stack requires a layer-wise description of the electrical field variables. For instance, Mitchell and Reddy (1995) formulated a 'hybrid' model in which an equivalent single layer kinematics has been employed with a layer-wise assumption for the electric potential. In general, different choices can be made for the electrical variables, which should ensure both a consistent representation of piezoelectric coupling and computational efficiency (Sze et al., 2004). As far as the in-plane distribution of the electrical field variables is concerned, the satisfaction of the equipotentiality condition across an electrode has been shown to be of primary relevance (Chevallier et al., 2008). It is finally mentioned that, as an alternative to coupled electromechanical models, dedicated purely mechanical finite elements (FEs) have been proposed by, e.g., Pablo et al. (2009) by including the piezoelectric effects into an equivalent mechanical stiffness and corresponding loading.

The above considerations on the modeling issues of composite structures with embedded piezoelectric materials are next employed to propose a literature review of FE formulations for piezoelectric shells. The review is limited to papers appeared after 2000, for previous developments we refer to the exhaustive survey of Benjeddou (2000). Only general shell formulations will be considered, which means that 'flat' elements like those developed for plates and axisymmetric shells will not be mentioned.

Several two-dimensional (2D) conventional shell elements have been formulated for the analysis of composite structures with embedded piezoelectric materials. Most of them employ the classical FSDT kinematics, like the 4-node elements by Lammering (1991), Lammering and Mesecke-Rischmann (2003), Zemčík et al. (2007), Zouari et al. (2009) and the 9-node elements by Balamurugan and Narayanan (2001, 2008) and Marinkovich et al. (2006). A third-order theory has been employed in the 8-node elements presented by Kulkarni and Bajoria (2003) and Varelis and Saravanos (2006). All aforementioned elements neglected the thickness change of the shell and employed, hence, the reduced 2D constitutive law. Six parameters per node have been used by Kulikov and Plotnikova (2008) for a 'geometrically exact' 4-node shell element and by Lee et al. (2003)

for a 9-node isoparametric shell element. These elements retained the full 3D constitutive law, which is an important feature for a consistent representation of complex physical interactions like multi-field coupling (Cho and Oh, 2003). However, the linear approximation for the transverse deflection used within the six parameters shell formulation is known to suffer the so-called Poisson locking (as detailed out by Carrera and Brischetto, 2008). In order to consistently resolve the coupling between membrane and stretching energy contributions, Kulikov and Plotnikova (2008) modified the 3D constitutive law and Lee et al. (2003) enriched the transverse strain distribution by referring to the Enhanced Assumed Strain (EAS) technique. While the aforementioned elements are based on equivalent single-layer descriptions, Kögl and Bucalem (2005) employed a layer-wise FSDT mechanics. Their 4- and 9-node elements presented the extension to piezoelectric shell elements of the Mixed Interpolation of Tensorial Components (MITC) technique for contrasting transverse shear locking. A hierarchic discrete-layer kinematics based on piece-wise linear approximations has been proposed by Heyliger et al. (1996) and Saravanos (1997) in conjunction with an 8-node shell element. The accuracy of this description could be improved upon increasing the number of numerical layers which subdivide the physical plies of the laminate. This formulation permitted the direct use of the full 3D constitutive law. Very often the electrostatic potential has been taken to vary linearly over the thickness of the piezoelectric plies (Balamurugan and Narayanan, 2001; Lee et al., 2003; Kulkarni and Bajoria, 2003; Marinkovich et al., 2006; Zemčík et al., 2007; Kulikov and Plotnikova, 2008). Kögl and Bucalem (2005) and Balamurugan and Narayanan (2008) retained the induced electric field by a layer-wise quadratic assumption for the electrostatic potential. Additionally, in view of the fulfillment of the equipotentiality condition across the electrodes, Balamurugan and Narayanan (2008) took the electric potential to be constant at the top and bottom of each piezoelectric ply. Heyliger et al. (1996) employed the hierarchic discrete-layer description for the electric potential variables as well, which permits to enhance the distribution of the electric field over the thickness by introducing fictitious numerical layers. Linear and refined approximations for the distributions of electrical field variables along the thickness have been compared by Lammering and Mesecke-Rischmann (2003).

Three-dimensional (3D) continuum-based piezoelectric shell elements have been proposed by Sze et al. (2000); Zheng et al. (2004); Tan and Vu-Quoc (2005); Yao and Lu (2005); Klinkel and Wagner (2006, 2008). This element type offers the possibility to easily implement the 3D constitutive law. Poisson locking has been circumvented by resorting to either the EAS technique (Zheng et al., 2004; Klinkel and Wagner, 2006, 2008) or

a hybrid stress formulation (Sze et al., 2000). The equi-potentiality condition on surface electrodes has been satisfied either by an element-wise constant interpolation for the electric potential (as in, e.g., Zheng et al., 2004), or by introducing an 'electric node' concept (Yao and Lu, 2005). Most element formulations retained a linear distribution of the electrostatic potential along the thickness direction. In this case, a stack of several elements is necessary to capture the induced electric field. 3D shell elements with a direct representation of the induced electric field employed a bilinear assumption for the electric field (Klinkel and Wagner, 2006, 2008), or a quadratic distribution for the electric potential (Yao and Lu, 2005). All aforementioned 3D shell elements resorted to the Assumed Natural Strain (ANS) technique to alleviate transverse shear locking.

This study proposes a conventional, 8-node shell element which fully retains the 3D constitutive law upon introduction of a quadratic assumption along the thickness of the transverse deflection. The classical FSDT kinematics, described by the three displacement components of the reference surface and the two rotations of the transverse fiber, is thus enriched by a thickness stretch described by adding the transverse displacements at the top and bottom faces of the laminate as independent variables. Therefore, all the seven nodal degrees of freedom (dof) of the proposed kinematics have a clear physical meaning. Based on the previous experience of Polit and Bruant (2006) and in order to limit computational cost, the electrostatic potential is taken to be constant across the element domain and to vary linearly over the thickness of each piezoelectric layer. Hence, the equipotentiality condition on surface electrodes can be readily satisfied and, when necessary, the bending induced electric field can be accounted for by subdividing the piezoelectric physical ply into several numerical layers. As a result, the number of electric potential dof per element depends on the number of piezoelectric layers in the composite stack and on the electrical boundary conditions. Finally, the element robustness has been enhanced by efficiently tackling the well-known locking phenomena. For this, the modified interpolation scheme proposed by Polit et al. (1994) is implemented, which is directly derived from the field consistency paradigm and avoids transverse shear locking and spurious zero-energy modes. By using the same methodology, the membrane locking can be alleviated as well.

This article is organized as follows: Next Section describes the geometry of the shell-like solid and the reference frames that are subsequently used to introduce the 2D model assumptions (section 'Description of the model') and the FE approximations (section 'The FE approximations'). The resulting element is validated in section 'Numerical results' by referring to well-known linear static problems of piezoelectric and composite shell structures. Finally, the conclusion summarizes the main findings.

## DESCRIPTION OF THE SHELL

This preliminary section is dedicated to the geometric description of the shell-like solid and to the different reference frames that will be used for constructing the finite shell element.

### Description of the Geometry

Let us consider a shell $\mathcal{C} = \Omega \times [-\frac{h}{2}, \frac{h}{2}]$ where $h$ is the constant thickness of the shell and $\Omega$ the middle surface. The description of the geometry of the shell is based on the Cartesian coordinates of the nodes and on the FE approximation over the elementary domain. For this, an 8-node quadrilateral FE will be used. Figure 1 illustrates the employed FE approximation and shows the different reference frames that will be used to describe the geometry and the mechanics of the shell-like body. These different bases are precised in Table 1. The global coordinates of any arbitrary point in the elementary domain
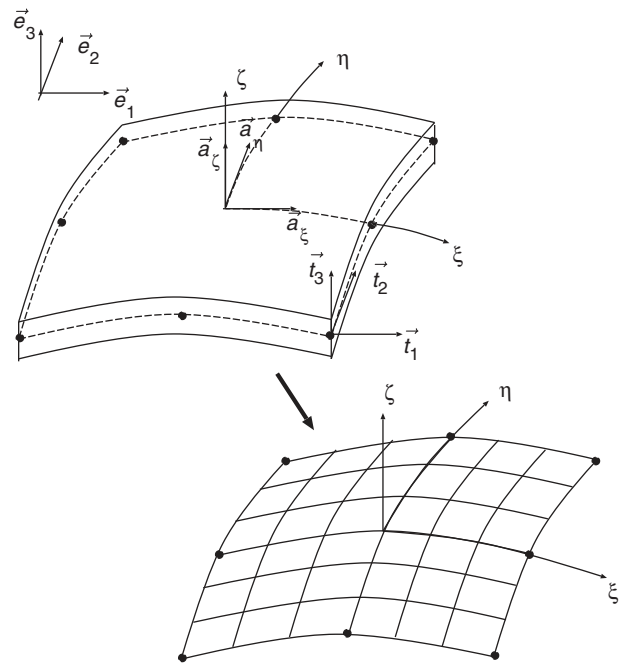


**Figure 1.** Description of the geometry of the 8-node shell element.

**Table 1. Reference frames used for the description of the shell.**

| | |
|---|---|
| $(\vec{e}_1, \vec{e}_2, \vec{e}_3)$ | Direct orthonormal Cartesian basis, (G) |
| $(X_1, X_2, X_3)$ | Global Cartesian coordinates |
| $(\vec{t}_1, \vec{t}_2, \vec{t}_3)$ | Direct orthonormal local basis, plane tangent to $\Omega$, (L) |
| $(x_1, x_2, z)$ | Local curvilinear coordinates on $\Omega$ |
| $(\vec{a}_\xi, \vec{a}_\eta, \vec{a}_3)$ | Reduced local basis, plane tangent to $\Omega$, (R) |
| $(\xi, \eta, \zeta)$ | Reduced curvilinear coordinates on $\Omega$ |

can be expressed in terms of the reduced (curvilinear) coordinates $\xi$, $\eta$ and the rectilinear normal coordinate $z$:

$$\vec{\Phi}(\xi,\eta,z) = \begin{bmatrix} X_1(\xi,\eta,z) \\ X_2(\xi,\eta,z) \\ X_3(\xi,\eta,z) \end{bmatrix} = \sum_{i=1}^{8} N_{q_i}(\xi,\eta) \begin{bmatrix} X_1 \\ X_2 \\ X_3 \end{bmatrix}_i$$
$$+ z \sum_{i=1}^{8} N_{q_i}(\xi,\eta) \begin{bmatrix} t_{31} \\ t_{32} \\ t_{33} \end{bmatrix}_i \tag{1}$$

where $z$ is related to the unit axis $\xi$ through a scalar coefficient, and $N_{q_i}(\xi,\eta)$ are the classical Serendipity interpolation functions.

The thickness of the shell is described in terms of the unit vector $\vec{t}_3 = [t_{31}\ t_{32}\ t_{33}]^T$ normal to the middle surface $\Omega$. We prescribe $\vec{t}_3 = \vec{a}_3$, i.e., the normal direction of the local curvilinear reference frame on $\Omega$ coincides with the normal direction of the local tangent plane to $\Omega$ (Figure 1). The covariant in-plane base vectors $\vec{a}_\alpha$ are usually obtained from the map $\vec{\Phi}$ introduced in Equation (1) to define the shell mid-surface $\Omega$:

$$\vec{a}_\alpha = \vec{\Phi}(\xi,\eta)_{,\alpha} \quad \text{for } \alpha = \xi,\eta \tag{2}$$

and the normal vector $\vec{t}_3 = \vec{a}_3$ is finally obtained from the perpendicularity condition:

$$\vec{t}_3 = \vec{a}_3 = \frac{\vec{a}_1 \wedge \vec{a}_2}{||\vec{a}_1 \wedge \vec{a}_2||} \tag{3}$$

The construction of the local base vectors $\vec{t}_1$ and $\vec{t}_2$ follows the procedure suggested by Zienkiewicz and Taylor (2000).

### The Change of Bases

The displacement field vector and the scalar electrostatic potential are expressed with respect to the global reference frame $\vec{e}_i$ as:

$$\begin{cases} \vec{u}(X_1,X_2,X_3,t) = \sum_{i=1}^{3} u_i^G(X_1,X_2,X_3,t)\vec{e}_i \\ \phi(X_1,X_2,X_3,t) \end{cases} \tag{4}$$

where the superscript $G$ indicates that the components are taken in the global reference frame. The displacement vector $[u] = [u_1\ u_2\ u_3]^T$ is expressed in the local orthonormal basis ($L$) by:

$$[u^L] = [T_{LG}][u^G] \text{ with } [T_{LG}] = \begin{bmatrix} t_{11} & t_{12} & t_{13} \\ t_{21} & t_{22} & t_{23} \\ t_{31} & t_{32} & t_{33} \end{bmatrix}$$
$$= \begin{bmatrix} \vec{t}_1 \cdot \vec{e}_1 & \vec{t}_1 \cdot \vec{e}_2 & \vec{t}_1 \cdot \vec{e}_3 \\ \vec{t}_2 \cdot \vec{e}_1 & \vec{t}_2 \cdot \vec{e}_2 & \vec{t}_2 \cdot \vec{e}_3 \\ \vec{t}_3 \cdot \vec{e}_1 & \vec{t}_3 \cdot \vec{e}_2 & \vec{t}_3 \cdot \vec{e}_3 \end{bmatrix} \tag{5}$$

In the same way, the following expression can be obtained:

$$[u^G] = [T_{GL}][u^L] \quad \text{with} \quad [T_{GL}] = [T_{LG}]^{-1}$$
$$= [T_{LG}]^T = \begin{bmatrix} t_{11} & t_{21} & t_{31} \\ t_{12} & t_{22} & t_{32} \\ t_{13} & t_{23} & t_{33} \end{bmatrix} \tag{6}$$

The displacement vector $[u^R]$ defined in the reduced local basis is constructed as:

$$[u^R] = [T_{RG}][u^G] \quad \text{with} \quad [T_{RG}] = \begin{bmatrix} a_{11} & a_{21} & a_{31} \\ a_{12} & a_{22} & a_{32} \\ a_{13} & a_{23} & a_{33} \end{bmatrix}$$
$$= \begin{bmatrix} \vec{a}_1 \cdot \vec{e}_1 & \vec{a}_1 \cdot \vec{e}_2 & \vec{a}_1 \cdot \vec{e}_3 \\ \vec{a}_2 \cdot \vec{e}_1 & \vec{a}_2 \cdot \vec{e}_2 & \vec{a}_2 \cdot \vec{e}_3 \\ \vec{a}_3 \cdot \vec{e}_1 & \vec{a}_3 \cdot \vec{e}_2 & \vec{a}_3 \cdot \vec{e}_3 \end{bmatrix} \tag{7}$$

Furthermore, the inverse relation holds:

$$[u^G] = [T_{GR}][u^R] \quad \text{with} \quad [T_{GR}] = [T_{RG}]^{-1} \tag{8}$$

Similar relations can be established between the local orthonormal $L$ and reduced $R$ reference frames by substituting $G$ by $L$.

## DESCRIPTION OF THE MODEL

The reduced 2D shell model is constructed starting from the classical *generalized displacement*-based variational formulation. The assumptions for the shell kinematics and the through-thickness distribution of the electrostatic potential are precised. A matrix notation is employed which facilitates the subsequent introduction of the FE approximations.

### The Weak Form of the Boundary Value Problem

The classical piezoelectric variational formulation of Tiersten (1969) is employed in which the primary field variables are the 'generalized displacements', i.e. the displacement field and the electrostatic potential. Using a matrix notation and for admissible virtual generalized displacements $u^*$ and $\phi^*$ (virtual quantities are denoted by an asterisk), the variational principle is given by:

$$\int_{\mathcal{C}} \rho[u^{L*}]^T[\ddot{u}^L]\,\mathrm{d}\mathcal{C} = -\int_{\mathcal{C}} [\varepsilon^{L*}(u^{L*})]^T[\sigma^L(u^L,\phi)]\,\mathrm{d}\mathcal{C}$$
$$+ \int_{\mathcal{C}} [u^{L*}]^T[f]\,\mathrm{d}\mathcal{C} + \int_{\partial\mathcal{C}_F} [u^{L*}]^T[F]\,\mathrm{d}\partial\mathcal{C}$$
$$+ \int_{\mathcal{C}} [E^{L*}(\phi^*)]^T[D^L(u^L,\phi)]\,\mathrm{d}\mathcal{C}$$
$$- \int_{\mathcal{C}} q\phi^*\,\mathrm{d}\mathcal{C} - \int_{\partial\mathcal{C}_Q} Q\phi^*\,\mathrm{d}\partial\mathcal{C} \tag{9}$$

where $[f]$ is the body force vector, $[F]$ the surface force vector applied on $\partial\mathcal{C}_F$, $q$ the volume charge density, $Q$ the surface charge density supplied on $\partial C_q$, and $\rho$ is the mass density. Finally, $\varepsilon^{L^*}(u^{L^*})$ and $E^*(\phi^*)$ are the virtual strain and virtual electric field that satisfy the compatibility gradient equations, while $\sigma^L$ and $D$ are the conjugated fluxes (stress and dielectric displacement, respectively) obtained from the constitutive equations. Note that the variational formulation is written in the local reference frame because the constitutive relation is described in this coordinate system (see the next section).

In the remainder of this article, we will refer only to static problems, for which the left-hand side term is set to zero. Furthermore, body forces and volume charge densities will be discarded ($[f]=[0]$; $q=0$).

**The Constitutive Equation**

The 3D constitutive equation for a linear piezoelectric material is given by the following set of coupled equations (ANSI/IEEE Std 176-1987, 1987):

$$[\sigma^L] = [C][\varepsilon^L] - [e]^T[E^L] \tag{10a}$$

$$[D^L] = [e][\varepsilon^L] + [\epsilon][E^L] \tag{10b}$$

where we denote by $[C]$ the matrix of elastic stiffness coefficients taken at constant electric field, by $[e]$ the matrix of piezoelectric stress coefficients and by $[\epsilon]$ the matrix of electric permittivity coefficients taken at constant strain. The explicit form of these matrices is given in appendix for an orthotropic piezoelectric layer working in 31-mode. Equation (10a) expresses the piezoelectric *converse* effect for actuator applications, whereas Equation (10b) represents the piezoelectric *direct* effect which is exploited in sensor applications. Note that the constitutive law is expressed in the local reference frame.

**The Displacement and Strain Fields**

The shell kinematics is based on the classical Reissner–Mindlin plate model, which is however enlarged by a quadratic thickness stretch displacement. An equivalent single-layer approach is employed for describing the kinematics of the composite cross-section. The displacement field can be expressed by:

$$\vec{u}^G(x_1, x_2, z) = \vec{v}^G(x_1, x_2) + z\vec{\beta}^L(x_1, x_2)$$
$$+ \vec{w}_{st}^L(x_1, x_2, z) \tag{11}$$

where the classical Reissner–Mindlin kinematics reads:

$$\vec{v}^G = v^G{}_1\,\vec{e}_1 + v^G{}_2\,\vec{e}_2 + v^G{}_3\,\vec{e}_3 \tag{12a}$$

$$\vec{\beta}^L = \theta^L{}_2\,\vec{t}_1 - \theta^L{}_1\,\vec{t}_2 \tag{12b}$$

The displacements $v^G{}_i$ are taken in the global frame with respect to the Cartesian $\vec{e}_i$ directions, while $\theta^L{}_\alpha$ ($\alpha = 1, 2$) are the positive rotations about the local axes $\vec{t}_\alpha$ of the transverse fiber initially normal to the shell mid-surface. The additional term $\vec{w}_{st}^L$ acts on the local direction normal to the shell surface. This stretching term is constructed as a Lagrange quadratic expansion of the local thickness coordinate $z$ as follows:

$$\vec{u}^G \cdot \vec{t}_3 = \left(\vec{v}^G + \vec{w}_{st}^L\right) \cdot \vec{t}_3 = f_m(z)\,w_m(x_1, x_2)$$
$$+ f_b(z)\,w_b(x_1, x_2) + f_t(z)\,w_t(x_1, x_2) \tag{12c}$$

where $w_m$, $w_b$, and $w_t$ are the displacements along $\vec{t}_3$ at the shell middle, bottom, and top surfaces, respectively, and

$$f_m(z) = 1 - \frac{4}{h^2}\,z^2 \qquad f_b(z) = \frac{1}{h}\,z\left(\frac{2}{h}z - 1\right)$$

$$f_t(z) = \frac{1}{h}\,z\left(\frac{2}{h}z + 1\right) \tag{12d}$$

Note that $w_m = \vec{v}^G \cdot \vec{t}_3$ and that this refinement needs only two additionally unknown functions ($w_b$ and $w_t$) with respect to the classical Reissner–Mindlin kinematics. For further convenience we introduce the following notation:

$$\vec{w} = \vec{u}^G \cdot \vec{t}_3 = w_0 + z\,w_1 + z^2\,w_2 \tag{13}$$

By virtue of this quadratic approximation, the full 3D constitutive equation can be directly employed with the present kinematics without Poisson locking problems (see also Carrera and Brischetto, 2008).

The compatible strain field is obtained from the linear strain-displacement relations, which in the global reference frame read:

$$\varepsilon^G{}_{ij}(\vec{u}^G) = \frac{1}{2}\left(\vec{u}^G{}_{,i} + \vec{u}^G{}_{,j}\right) \tag{14}$$

where $i, j = X_1, X_2$, and $X_3$. The components of the strain tensor can be calculated with respect to the three bases $G$, $L$, and $R$:

$$\varepsilon(\vec{u}^G) = \varepsilon^G{}_{ij}(\vec{e}^i \otimes \vec{e}^j) = \varepsilon^L{}_{ij}(\vec{t}^i \otimes \vec{t}^j)$$
$$= \varepsilon^{Rij}(\vec{a}_i \otimes \vec{a}_j) = \varepsilon^R{}_{ij}(\vec{a}^i \otimes \vec{a}^j) \tag{15}$$

It must be noted that covariant and contravariant components are the same when expressed with respect to an orthonormal basis, for example $\vec{e}_i$ and $\vec{t}_i$. This is not the case when the strain components are expressed in the local reduced reference frame $\vec{a}_i$. Therefore, we can express the strain tensor in the reduced basis in either covariant or contravariant components.

In this study, the strain components are first calculated from the FE approximations with respect to the reduced local basis vectors. This allows us to carry out the special treatment to correct the membrane and transverse shear locking described in Section 'Correction of the transverse shear and membrane locking'. The strains are subsequently expressed in the local orthonormal reference frame through the opportune basis transformations (Section 'Strain components in the local basis'). As already mentioned, the local reference frame is the correct one in which the constitutive law should be expressed.

Based on the above considerations, and for further convenience, we express the local strain from Equations (11) and (15) by separating the contributions that are constant, linear, and quadratic in the thickness coordinate $z$:

$$[\varepsilon^L] = [\varepsilon^{L0}] + z[\varepsilon^{L1}] + z^2[\varepsilon^{L2}] \tag{16}$$

Additionally, the following expression can be deduced by rearranging the thickness assumption in the matrix $[F_\varepsilon(z)]$ and by separating the contributions of the in-plane strains $\varepsilon_p$, the transverse shear strains $\gamma$ and the transverse stretch $\varepsilon_{33}$:

$$[\varepsilon^L] = \begin{bmatrix} [\varepsilon_p^L] \\ [\gamma^L] \\ [\varepsilon_{33}^L] \end{bmatrix} = [F_\varepsilon(z)][\varepsilon_u] \tag{17}$$

## The Electric Potential and the Electric Field Vector

A layer-wise linear approximation is used to describe the through-thickness behavior of the scalar electrostatic potential $\phi(x_1, x_2, z)$. There are two main advantages of this layer-wise description:

- independent electrical boundary conditions can be applied to each piezoelectric ply;
- a refinement of the description of the electric field variable is easily obtained by subdividing the physical piezoelectric ply into several numerical layers.

As pointed out in the literature review, the latter point is particularly important when dealing with problems involving a bending-induced electric field along the shell thickness (see, e.g., Klinkel and Wagner, 2006; Polit and Bruant, 2006).

For a layer $(k)$ with a thickness $e^{(k)}$ and a reduced normal coordinate $\zeta \in [-1, 1]$, we have a linear variation using two potential values $(\phi_{bot}^{(k)}, \phi_{top}^{(k)})$ located at the bottom and top of each layer:

$$\phi^{(k)}(x_1, x_2, z(\zeta)) = \frac{1}{2}(1 - \zeta)\phi_{bot}^{(k)}(x_1, x_2)$$
$$+ \frac{1}{2}(1 + \zeta)\phi_{top}^{(k)}(x_1, x_2) \tag{18}$$

The expression in the local reference frame with $z \in [z_{bot}^{(k)}, z_{top}^{(k)}]$ is obtained by considering the relation between the coordinates:

$$z(\zeta) = \frac{1}{2}(z_{bot}^{(k)} + z_{top}^{(k)}) + \frac{1}{2}\zeta e^{(k)} \tag{19}$$

The matrix notation introduced in Equation (17) is employed for the electric potential as well:

$$[\phi^{(k)}(x_1, x_2, z(\zeta))] = [F_\phi^{(k)}(z)] \begin{bmatrix} \phi_{bot}^{(k)}(x_1, x_2) \\ \phi_{top}^{(k)}(x_1, x_2) \end{bmatrix} \tag{20}$$

The electric field vector $[E^{L(k)}] = [E_{x_1}^{L(k)} \; E_{x_2}^{L(k)} \; E_z^{L(k)}]^T$ is obtained from the gradient relation:

$$-[E^{L(k)}(x_1, x_2, z(\zeta))] = \begin{bmatrix} \phi_{,1}^{(k)} \\ \phi_{,2}^{(k)} \\ \phi_{,3}^{(k)} \end{bmatrix} = [F_E^{(k)}(z)][E_\phi^{(k)}] \tag{21a}$$

where $[E_\phi^{(k)}]$ contains the derivatives of the approximation for $\phi^{(k)}$ given in Equation (18):

$$[E_\phi^{(k)}] = \begin{bmatrix} \phi_{bot}^{(k)}(x_1, x_2) \\ \phi_{bot}^{(k)}(x_1, x_2)_{,1} \\ \phi_{bot}^{(k)}(x_1, x_2)_{,2} \\ \phi_{top}^{(k)}(x_1, x_2) \\ \phi_{top}^{(k)}(x_1, x_2)_{,1} \\ \phi_{top}^{(k)}(x_1, x_2)_{,2} \end{bmatrix} \tag{21b}$$

More details about the expressions of the matrices $[F_E^{(k)}(z)]$ and $[F_\phi^{(k)}(z)]$ have been reported by Polit and Bruant (2006).

## The Reduced 2D Problem

Taking into account the constitutive law in Equation (10), the variational principle expressed by Equation (9) reads (inertia terms, body forces, and volume charge densities are discarded):

$$\int_C \left\{ [\varepsilon^{L*}(u^{L*})]^T ([C][\varepsilon^L(u^L)] - [e]^T[E^L(\phi)]) \right.$$
$$\left. - [E^{L*}(\phi^*)]^T ([e][\varepsilon^L(u^L)] + [\epsilon][E^L(\phi)]) \right\} \, dC = W_{ext}^* \tag{22}$$

where $W_{ext}^*$ represents the external virtual work done by the prescribed surface traction $[F]$ and charge densities $[Q]$. The model assumptions for the kinematics (Equation (17)) and the electric field (Equation (21a)) are further introduced by considering the quantities

specific to the layer ($k$). As a result, the dependency on the thickness coordinate $z$ explicitly appears in the governing equation (22) and the integral over the domain $\mathcal{C}$ can be written as

$$
\int_{\Omega}\left[\varepsilon_u^*\right]^T\left\{\int_h[F_\varepsilon(z)]^T[C^{(k)}][F_\varepsilon(z)]\mathrm{d}z\right\}[\varepsilon_u]\,\mathrm{d}\Omega
$$
$$
+\int_{\Omega}\left[\varepsilon_u^*\right]^T\left\{\int_h[F_\varepsilon(z)]^T[e^{(k)}]^T\left[F_E^{(k)}(z)\right]\mathrm{d}z\right\}\left[E_\phi^{(k)}\right]\mathrm{d}\Omega
$$
$$
+\int_{\Omega}\left[E_\phi^{(k)*}\right]^T\left\{\int_h\left[F_E^{(k)}(z)\right]^T[e^{(k)}][F_\varepsilon(z)]\mathrm{d}z\right\}[\varepsilon_u]\,\mathrm{d}\Omega
$$
$$
-\int_{\Omega}\left[E_\phi^{(k)*}\right]^T\left\{\int_h\left[F_E^{(k)}(z)\right]^T[\epsilon^{(k)}]\left[F_E^{(k)}(z)\right]\mathrm{d}z\right\}\left[E_\phi^{(k)}\right]\mathrm{d}\Omega
$$
$$
= W_{ext}^* \tag{23}
$$

The integral over the thickness of the multilayered shell is carried out by considering the separate layer contributions. Since an equivalent single layer description is employed for the kinematics, the mechanical stiffness term is computed as the sum over the contributions of all layers:

$$
[k_{uu}] = \sum_k[k_{uu}^{(k)}] = \sum_k\left\{\int_{h_k}[F_\varepsilon(z)]^T[C^{(k)}][F_\varepsilon(z)]\mathrm{d}z\right\} \tag{24}
$$

The matrix $[k_{uu}]$ is thus square with dimensions independent of the number of layers. On the contrary, a layer-wise description is used for the electric field and an assembly procedure is necessary for constructing the dielectric matrix for the whole multilayered shell:

$$
[k_{\phi\phi}] = \bigcup_k\left[k_{\phi\phi}^{(k)}\right]
$$
$$
= \bigcup_k\left\{\int_{h_k}\left[F_E^{(k)}(z)\right]^T[\epsilon^{(k)}]\left[F_E^{(k)}(z)\right]\mathrm{d}z\right\} \tag{25}
$$

Therefore, the matrix $[k_{\phi\phi}]$ is square with dimensions that depend on the number of layers into which the shell is subdivided. The piezoelectric coupling terms finally arise from the second and third terms of Equation (23):

$$
\left[k_{u\phi}^{(k)}\right] = \int_{h_k}[F_\varepsilon(z)]^T[e^{(k)}]^T\left[F_E^{(k)}(z)\right]\mathrm{d}z \tag{26a}
$$

$$
\left[k_{\phi u}^{(k)}\right] = \int_{h_k}\left[F_E^{(k)}(z)\right]^T[e^{(k)}][F_\varepsilon(z)]\mathrm{d}z = \left[k_{u\phi}^{(k)}\right]^T \tag{26b}
$$

The construction of the coupling matrix $[k_{u\phi}]$ for the whole multilayered shell involves, hence, the summation over the layers for the rows and the assembly procedure for the columns, which yields a rectangular matrix whose number of columns depends on the number of layers. The coupling matrix $[k_{\phi u}]$ is evidently obtained as:

$$
[k_{\phi u}] = [k_{u\phi}]^T \tag{27}
$$

Having eliminated the dependency on the thickness coordinate $z$ from Equation (23), the reduced 2D problem on $\Omega$ finally reads:

$$
\int_{\Omega}\left[\varepsilon_u^*\right]^T\left([k_{uu}][\varepsilon_u] + [k_{u\phi}]\left[E_\phi^{(k)}\right]\right) + \left[E_\phi^{(k)*}\right]^T
$$
$$
\times\left([k_{u\phi}]^T[\varepsilon_u] - [k_{\phi\phi}]\left[E_\phi^{(k)}\right]\right)\mathrm{d}\Omega = W_{ext}^* \tag{28}
$$

## THE FE APPROXIMATIONS

This section introduces the FE approximations for the mechanical and the electrical field variables as well as the dedicated treatment to avoid locking problems. The solution of the resulting discrete form of the coupled electromechanical system is finally discussed in Section 'The discrete piezoelectric system'.

### The FE Approximation for the Mechanical Variables

Based on the 8-node shell element illustrated in Figure 2, the following FE approximation can be introduced for the kinematics:

$$
\vec{u}^G = \sum_i N_{q_i}(\xi,\eta)\left(\vec{v}^G\right)_i + z\sum_i N_{q_i}(\xi,\eta)\left(\vec{\beta}^L\right)_i
$$
$$
+ \sum_i N_{q_i}(\xi,\eta)\left(\vec{w}_{st}^L\right)_i \tag{29}
$$

The vector of the dof of the element is thus introduced according to $[q^L{}_e]^T = [v^G{}_1\ v^G{}_2\ v^G{}_3\ \theta^L{}_1\ \theta^L{}_2\ w_1\ w_2]_{i=1,\dots,8}$

### The Strain Field

In view of the subsequent introduction of the corrections of the locking problems, we first express the strain field in the reduced local basis as:

$$
\varepsilon^R{}_{ij} = \frac{1}{2}\left(\vec{u}^G{}_{,i}\cdot\vec{a}_j + \vec{u}^G{}_{,j}\cdot\vec{a}_i\right) \tag{30}
$$

where $i, j = 1, 2, 3$ stand for $\xi, \eta, \zeta$, i.e., the reduced coordinates of the FE approximation. The in-plane,
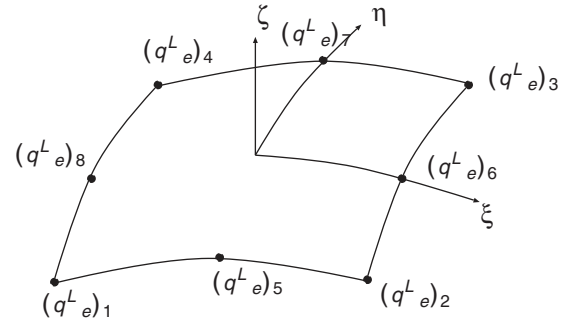


**Figure 2.** The 8-node shell FE.

transverse shear and transverse normal strains introduced in Equation (17) can be written as:

$$\left[\varepsilon_p^R\right] = \left[\varepsilon_p^{R0}\right] + z\left[\varepsilon_p^{R1}\right] = \begin{bmatrix} \varepsilon^0{}_{\xi\xi} \\ \varepsilon^0{}_{\eta\eta} \\ \gamma^0{}_{\xi\eta} \end{bmatrix} + z\begin{bmatrix} \varepsilon^1{}_{\xi\xi} \\ \varepsilon^1{}_{\eta\eta} \\ \gamma^1{}_{\xi\eta} \end{bmatrix} \quad (31a)$$

$$\left[\gamma^R\right] = \left[\gamma^{R0}\right] + z\left[\gamma^{R1}\right] + z^2\left[\gamma^{R2}\right]$$
$$= \begin{bmatrix} \gamma^0{}_{\eta3} \\ \gamma^0{}_{\xi3} \end{bmatrix} + z\begin{bmatrix} \gamma^1{}_{\eta3} \\ \gamma^1{}_{\xi3} \end{bmatrix} + z^2\begin{bmatrix} \gamma^2{}_{\eta3} \\ \gamma^2{}_{\xi3} \end{bmatrix} \quad (31b)$$

$$\left[\varepsilon_{33}^L\right] = \left[\varepsilon_{33}^{L0}\right] + z\left[\varepsilon_{33}^{L1}\right] \quad (31c)$$

Note that since $\vec{a}_3 = \vec{t}_3$ we have $[\epsilon_{33}^L] = [\epsilon_{33}^R]$, i.e., the transverse normal strain in the reduced basis coincides with Equation (31c). In the following, the relation between the separate strain contributions and the assumed kinematics are explicitly reported.

$$[BC_i] = \begin{bmatrix} \vec{a}_3 \cdot \vec{e}_1 \ N_{q_i,\eta} & \vec{a}_3 \cdot \vec{e}_2 \ N_{q_i,\eta} & \vec{a}_3 \cdot \vec{e}_3 \ N_{q_i,\eta} & -\vec{a}_2 \cdot \vec{t}_2 \ N_{q_i} & \vec{a}_2 \cdot \vec{t}_1 \ N_{q_i} \\ \vec{a}_3 \cdot \vec{e}_1 \ N_{q_i,\xi} & \vec{a}_3 \cdot \vec{e}_2 \ N_{q_i,\xi} & \vec{a}_3 \cdot \vec{e}_3 \ N_{q_i,\xi} & -\vec{a}_1 \cdot \vec{t}_2 \ N_{q_i} & \vec{a}_1 \cdot \vec{t}_1 \ N_{q_i} \end{bmatrix} \quad (34b)$$

## MEMBRANE STRAIN $\left[\varepsilon_p^{R0}\right]$

The membrane strain term is defined by:

$$\left[\varepsilon_p^{R0}\right] = \sum_i [BMPM_i] \begin{bmatrix} v^G{}_1 \\ v^G{}_2 \\ v^G{}_3 \end{bmatrix}_i \quad (32a)$$

with

$$[BMPM_i] =$$
$$\begin{bmatrix} \vec{a}_1 \cdot \vec{e}_1 \ N_{q_i,\xi} & \vec{a}_1 \cdot \vec{e}_2 \ N_{q_i,\xi} & \vec{a}_1 \cdot \vec{e}_3 \ N_{q_i,\xi} \\ \vec{a}_2 \cdot \vec{e}_1 \ N_{q_i,\eta} & \vec{a}_2 \cdot \vec{e}_2 \ N_{q_i,\eta} & \vec{a}_2 \cdot \vec{e}_3 \ N_{q_i,\eta} \\ \vec{a}_2 \cdot \vec{e}_1 \ N_{q_i,\xi} & \vec{a}_2 \cdot \vec{e}_2 \ N_{q_i,\xi} & \vec{a}_2 \cdot \vec{e}_3 \ N_{q_i,\xi} \\ +\vec{a}_1 \cdot \vec{e}_1 \ N_{q_i,\eta} & +\vec{a}_1 \cdot \vec{e}_2 \ N_{q_i,\eta} & +\vec{a}_1 \cdot \vec{e}_3 \ N_{q_i,\eta} \end{bmatrix} \quad (32b)$$

where $\vec{a}_\alpha$ are evaluated at the integration points.

## BENDING STRAIN $\left[\varepsilon_p^{R1}\right]$

For the bending contribution associated to the rotations $\theta^L{}_\alpha$ ($\alpha = 1, 2$), the scalar product must be considered between the local base vectors $\vec{t}_\alpha$ and the reduced basis. We have thus:

$$\left[\varepsilon_p^{R1}\right] = \sum_i [BF_i] \begin{bmatrix} \theta^L{}_1 \\ \theta^L{}_2 \end{bmatrix}_i \quad (33a)$$

with

$$[BF_i] = \begin{bmatrix} -\vec{a}_1 \cdot \vec{t}_2 \ N_{q_i,\xi} & \vec{a}_1 \cdot \vec{t}_1 \ N_{q_i,\xi} \\ -\vec{a}_2 \cdot \vec{t}_2 \ N_{q_i,\eta} & \vec{a}_2 \cdot \vec{t}_1 \ N_{q_i,\eta} \\ -\vec{a}_2 \cdot \vec{t}_2 \ N_{q_i,\xi} & \vec{a}_2 \cdot \vec{t}_1 \ N_{q_i,\xi} \\ -\vec{a}_1 \cdot \vec{t}_2 \ N_{q_i,\eta} & +\vec{a}_1 \cdot \vec{t}_1 \ N_{q_i,\eta} \end{bmatrix} \quad (33b)$$

Here, the $\vec{a}_\alpha$ are evaluated at the integration points while $\vec{t}_\alpha$ are evaluated at the node.

## CONSTANT TRANSVERSE SHEAR STRAIN $[\gamma^{R0}]$

For the constant part of the transverse shear strain, both the scalar products must be considered that project the global and local bases with respect to the reduced basis. We have:

$$[\gamma^{R0}] = \sum_i [BC_i] \begin{bmatrix} v^G{}_1 \\ v^G{}_2 \\ v^G{}_3 \\ \theta^L{}_1 \\ \theta^L{}_2 \end{bmatrix}_i \quad (34a)$$

with

In this last equation, $\vec{a}_i$ are evaluated at the integration points while $\vec{t}_\alpha$ are evaluated at the node.

## NON-CONSTANT TRANSVERSE SHEAR STRAIN $[\gamma^{R1}]$ AND $[\gamma^{R2}]$

The linear and quadratic terms of the transverse shear strain are associated to the linear and quadratic terms of the assumption Equation (13), respectively. The expression for these contributions thus reads:

$$\gamma_{\alpha3}^{R1} = \sum_i N_{q_i,\alpha}(w_1)_i \quad \text{and}$$
$$\gamma_{\alpha3}^{R2} = \sum_i N_{q_i,\alpha}(w_2)_i \quad (\alpha \in \{\xi, \eta\}) \quad (35)$$

## TRANSVERSE NORMAL STRAIN $\left[\varepsilon_{33}^{L0}\right]$ AND $\left[\varepsilon_{33}^{L1}\right]$

The constant and linear contributions of the transverse normal strain can be directly obtained from Equation (13) as:

$$\varepsilon_{33}^{L0} = \sum_i N_{q_i}(w_1)_i \quad \text{and} \quad \varepsilon_{33}^{L1} = \sum_i 2 N_{q_i}(w_2)_i \quad (36)$$
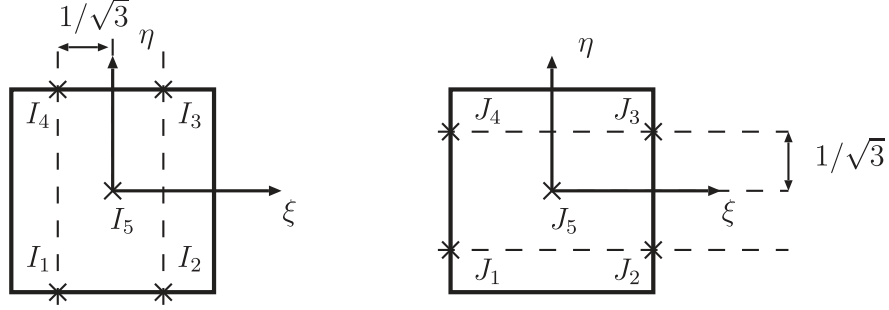
**Figure 3.** *Point locations for the transverse shear strain evaluations.*

**Correction of the Transverse Shear and Membrane Locking**

In the following, the special treatment of the transverse shear and membrane strains is presented, by which the numerical locking problems are alleviated. The methodology is based on the field consistency paradigm and a previous implementation has already demonstrated its efficiency for plates (Polit et al., 1994) and shells (Polit and Touratier, 1999). In order to obtain best performances even in presence of distorted meshes, the field consistency is ensured in the local reduced coordinate system.

*TRANSVERSE SHEAR STRAIN INTERPOLATIONS*

Transverse shear locking is caused by the constant part of the transverse shear strain $[\gamma^0]$, in particular by the polynomial inconsistency of its isoparametric definition given in Equation (34) the quadratic contributions of the rotational dof $\theta^L_\alpha$ ($\alpha = 1, 2$) do not match the contributions obtained from the derivation of the local transverse displacement of the mid-surface $w_0$ (obtained from $(v^G_i)_{i=1,2,3}$). The procedure to avoid transverse shear locking is thus based on the construction of a new approximation for the constant part of the transverse shear strains and consists of the following steps:

- The transverse shear strains are defined in the local reduced coordinates:

$$\gamma^0_{\xi3} = \beta_\xi + w_{0,\xi} \quad \gamma^0_{\eta3} = \beta_\eta + w_{0,\eta} \quad (37)$$

where $\beta_\xi$, $\beta_\eta$ are the rotations in reduced coordinates obtained from the positive rotations $\theta_\alpha$ ($\alpha = 1, 2$), see also Equation (12b).
- In order to ensure the same polynomial approximation for the rotation and the transverse displacement in Equation (37), $w_0$ is assumed to be cubic, introducing four supplementary dof at the mid-side nodes: $(w_{0,\xi})_5$, $(w_{0,\eta})_6$, $(w_{0,\xi})_7$, $(w_{0,\eta})_8$.

- A linear variation of the tangential transverse shear strain component is assumed on each side of the elementary domain (Figure 2). Thus, the supplementary dof introduced at the previous step can be expressed as a linear combination of the rotation and transverse displacement values. Therefore, a new FE approximation is obtained for the transverse displacement $w_0$.
- The interpolation of the reduced transverse shear strain components is defined in the following polynomial bases, which represent the intersection sets of monomial terms from $\xi$ and $\eta$:

$$\mathcal{B}(\gamma^0_{\xi3}) = \mathcal{B}(\beta_\xi) \cap \mathcal{B}(w_{0,\xi}) = \{1, \xi, \eta, \xi\,\eta, \eta^2\} \quad (38a)$$

$$\mathcal{B}(\gamma^0_{\eta3}) = \mathcal{B}(\beta_\eta) \cap \mathcal{B}(w_{0,\eta}) = \{1, \xi, \eta, \xi\,\eta, \xi^2\} \quad (38b)$$

- According to the dimension of the polynomial basis, five points are needed for each reduced transverse shear strain. These points were chosen as indicated in Figure 3 because this location gives the best results in the case of distorted meshes (for more details see Polit et al., 1994). The following FE approximation is finally obtained for the reduced transverse shear strains:

$$\gamma^0_{\xi3}(\xi, \eta) = \sum_{I=1}^{5} C\xi_I(\xi, \eta)\gamma_{\xi I}$$

$$\gamma^0_{\eta3}(\xi, \eta) = \sum_{J=1}^{5} C\eta_J(\xi, \eta)\gamma_{\eta J} \quad (39)$$

This modified interpolation for the transverse shear strain substitutes that of Equation (34).

*MEMBRANE STRAIN INTERPOLATIONS*

The construction of a new consistent approximation for the membrane strain field is based on the same

arguments outlined in the previous section. The membrane strain terms $\left[\tilde{\varepsilon}_p^{R0}\right]$ in the local basis read:

$$\left[\tilde{\varepsilon}_p^{R0}\right] = \begin{bmatrix} \varepsilon^0_{\xi\xi} \\ \varepsilon^0_{\eta\eta} \\ \varepsilon^0_{\xi\eta} \\ \varepsilon^0_{\eta\xi} \end{bmatrix} = \begin{bmatrix} v_{\xi,\xi} \\ v_{\eta,\eta} \\ v_{\xi,\eta} \\ v_{\eta,\xi} \end{bmatrix} \qquad (40)$$

If the isoparametric approach is used, these membrane strain interpolations refer to incomplete second-order polynomials. Therefore, a consistent polynomial for the interpolation of $\left[\tilde{\varepsilon}_p^{R0}\right]$ is chosen by adopting the following set of monomial terms: $\{1, \xi, \eta, \xi\,\eta\}$. This polynomial basis requires four points for evaluating each membrane strain component, two in the $\xi$ direction and two in the $\eta$ direction. Numerical plate membrane tests with distorted meshes indicate that the best choice is to take the reduced integration points $K_1, \ldots, K_4$ illustrated in Figure 4. The new interpolation of each membrane strain component is thus given by:

$$\varepsilon_{\alpha\beta}(\xi,\eta) = \sum_{K=1}^{4} C\xi\eta_K(\xi,\eta)\varepsilon_{\alpha\beta K} \quad \text{for} \quad (\alpha,\beta) \in \{\xi,\eta\}^2 \quad (41)$$

This interpolation substitutes the isoparametric one in Equation (32).

**Strain Components in the Local Basis**

The strains defined in Equations (32)–(35) being expressed in the reduced basis, a tensorial transformation is necessary in order to express these strains in the physical local basis. The tensorial transformation is performed as:

$$\left[\varepsilon_p^{L\alpha}\right] = [TT_{LR}]\left[\varepsilon_p^{R\alpha}\right], \ \alpha = 0, 1 \qquad (42a)$$

$$\left[\gamma^{L\alpha}\right] = [T_{LR}]\left[\gamma^{R\alpha}\right], \ \alpha = 0, 1, 2 \qquad (42b)$$

where the second-order tensorial matrix:

$$[TT_{LR}] = \begin{bmatrix} T_{LR}(1,1)^2 & T_{LR}(1,2)^2 & T_{LR}(1,1)\,T_{LR}(1,2) \\ T_{LR}(2,1)^2 & T_{LR}(2,2)^2 & T_{LR}(2,1)\,T_{LR}(2,2) \\ 2\,T_{LR}(1,1)\,T_{LR}(2,1) & 2\,T_{LR}(1,2)\,T_{LR}(2,2) & T_{LR}(1,1)\,T_{LR}(2,2) + T_{LR}(1,2)\,T_{LR}(2,1) \end{bmatrix} \qquad (43a)$$

is constructed from the following transformation matrix:

$$[T_{LR}] = [T_{RL}]^{-1} \quad \text{with} \quad [T_{RL}] = \begin{bmatrix} \vec{a}_1 \cdot \vec{t}_1 & \vec{a}_1 \cdot \vec{t}_2 \\ \vec{a}_2 \cdot \vec{t}_1 & \vec{a}_2 \cdot \vec{t}_2 \end{bmatrix} \qquad (43b)$$
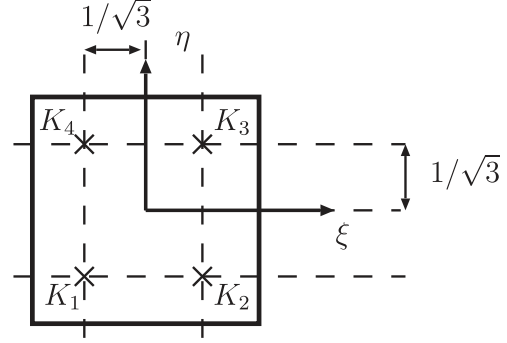


**Figure 4.** Point locations for the membrane strains evaluations.

**The FE Approximation for the Electric Potential**

We assume that the electric potential remains constant across the element coordinates $(\xi, \eta)$:

$$\phi(\xi,\eta) = \phi_e \qquad (44)$$

This choice allows us to develop a simple numerical tool which can be used in conjunction with active control algorithms and optimization processes. The previous study by Polit and Bruant (2006) has demonstrated that this approach yields good results. Moreover, it permits to easily enforce the equipotentiality condition at piezoelectric patch electrodes. Upon introduction of Equation (44) into Equation (21b), the in-plane derivatives of the electric potential terms vanish and a very simple expression is obtained for the array $[E_\phi^{(k)}]$:

$$[E_\phi^{(k)}] = [B_{const}\phi][q_{\phi_e}^{(k)}] \qquad (45)$$

where $[B_{const}\phi]$ contains only constant terms and the vector of the elementary electric dof contains the electric potential values at the top and bottom of the layer $(k)$:

$$[q_{\phi_e}^{(k)}] = \begin{bmatrix} q_{\phi_{e_{bot}}}^{(k)} \\ q_{\phi_{e_{top}}}^{(k)} \end{bmatrix} \qquad (46)$$

**The Discrete Piezoelectric System**

The FE interpolations on $\Omega$ for the strains given in Equations (33), (35), (36), (39), (41) and those for the electric field in Equation (45) are introduced in the 2D governing equation (28). The local orthonormal basis is addressed by referring to the transformations given in Equation (42). The integral over the elementary domain is carried out by means of the Gauss quadrature scheme. Assembling each elementary contribution in the global reference frame, the following discrete form of the coupled piezoelectric system is obtained:

$$\begin{bmatrix} [K_{uu}] & [K_{u\phi}] \\ [K_{u\phi}]^T & [K_{\phi\phi}] \end{bmatrix} \begin{bmatrix} [q_u] \\ [q_\phi] \end{bmatrix} = \begin{bmatrix} [L_u] \\ [L_\phi] \end{bmatrix} \quad (47)$$

where $[K_{uu}]$, $[K_{\phi\phi}]$, and $[K_{u\phi}]$ are the global stiffness, dielectric, and piezoelectric matrices of the shell, respectively. The mechanical dof (displacements and rotations) are included in the vector $[q_u]$, while the electrical dof (electric potentials) are in the vector $[q_\phi]$. The load vectors $[L_u]$ and $[L_\phi]$ represent the external loading from applied forces and prescribed charges, respectively. Essential boundary conditions (i.e., prescribed displacements and electric potentials) are imposed numerically by a penalty technique. The coupled system is then solved by the classical static condensation procedure for the electrical dof:

$$[q_\phi] = [K_{\phi\phi}]^{-1}([L_\phi] - [K_{u\phi}]^T[q_u]) \quad (48a)$$

which yields the following purely mechanical system with a modified equivalent stiffness matrix:

$$\begin{aligned} & \left[[K_{uu}] - [K_{u\phi}][K_{\phi\phi}]^{-1}[K_{u\phi}]^T\right][q_u] \\ & = [L_u] - [K_{u\phi}][K_{\phi\phi}]^{-1}[L_\phi] \end{aligned} \quad (48b)$$

**NUMERICAL RESULTS**

In this section, several tests available in open literature are presented in order to evaluate the efficiency of the present C7CL8PZ element (laminated shell element with seven mechanical dof per node, based on the CL8 strain interpolations of Polit et al. (1994) and including piezoelectric coupling). Flat plates are considered in Section 'Piezoelectric bimorph plate', open- and closed-cylindrical shell geometries are addressed in Section 'Closed cylindrical rings' and Section 'Composite cylindrical shell panels', respectively. Different stacking sequences are also included in this study in order to demonstrate the capabilities of the present piezoelectric composite shell element. Linear static actuator and sensor applications are discussed. For the sake of brevity, the robustness of the element with respect to transverse shear and membrane locking problems will not be assessed since this result has been already presented by Polit et al. (1994) and Polit and Touratier (1999).

We have chosen the case studies among those that have been more often reported in literature. A complete description in a unified format of the case studies is proposed so that there is no need to retrieve the original articles reported in the references. For compatibility with the reported references, the results will be often provided in graphical format. A new reference solution issued from a 3D FE simulation performed with the commercial software ANSYS is provided for those cases for which an uncertainty exists in the graphical evaluation of the reference results.

The results of the present element are compared with those obtained by other piezoelectric shell finite elements. Reference will be made to the element ISOP4 of Sze et al. (2000), the ISOP9 of Lee et al. (2003), the GEXP4 proposed by Kulikov and Plotnikova (2008) as well as to the elements denoted S-1997 (Saravanos, 1997), BN-2001 (Balamurugan and Narayanan, 2001), TVQ-2005 (Tan and Vu-Quoc, 2005) and BN-2008 (Balamurugan and Narayanan, 2008). All these elements employ the electrostatic potential as electrical dof. Table 2 summarizes the main features of these shell elements, namely the number of mechanical dof per node as well as the through-thickness assumptions and the FE approximations used for the electric potential. The notation LW (layer-wise) is employed if the assumption for the electric potential can be refined upon introduction of numerical interfaces.

*Table 2. Main features of the finite shell elements used for the numerical assessment.*

| Shell FE | Mechanical dof per node | Thickness electric approximation | In-plane electric approximation |
|---|---|---|---|
| S-1997 (Saravanos, 1997) | 5 | LW linear | Quadratic |
| ISOP4 (Sze et al., 2000) | 3 | Linear | Bilinear |
| BN-2001 (Balamurugan and Narayanan, 2001) | 5 | Linear | Constant |
| ISOP9 (Lee et al., 2003) | 6 | Linear | Biquadratic |
| TVQ-2005 (Tan and Vu-Quoc, 2005) | 3 | Linear | Bilinear |
| GEXP4 (Kulikov and Plotnikova, 2008) | 6 | Linear | Bilinear |
| BN-2008 (Balamurugan and Narayanan, 2008) | 5 | Quadratic | Constant[a] |
| C7CL8PZ (this study) | 7 | LW Linear | Constant |

[a]In the BN-2008 element, the electric potential is element-wise constant at the outer surfaces of the piezoelectric layer, while a biquadratic interpolation is used for the induced electric potential at the middle surface.

## Piezoelectric Bimorph Plate

The first numerical validation concerns the bimorph pointer illustrated in Figure 5, for which experimental results and an analytical solution have been provided by Tzou et al. (1990) and Tzou (1993), respectively. This experiment has been widely used in literature to validate the static response of piezoelectric shell elements.

**Geometry:** The bimorph consists of a rectangular plate with length $a = 100$ mm, width $b = 5$ mm, and thickness $h = 1$ mm (Figure 5).

**Material:** The bimorph consists of a stack of two PVDF layers with opposite polarization (bimorph in series or anti-parallel configuration, see also Fernandes and Pouget, 2003), which have the following properties:

| | | |
|---|---|---|
| $E_1 = 2$ GPa | $\nu_{12} = 0$ | $G_{12} = 1$ GPa |
| $E_2 = 2$ GPa | $\nu_{13} = 0$ | $G_{13} = 1$ GPa |
| $E_3 = 2$ GPa | $\nu_{23} = 0$ | $G_{23} = 1$ GPa |
| $e_{31} = 0.046$ C/m$^2$ | $e_{32} = 0.046$ C/m$^2$ | $e_{33} = 0$ C/m$^2$ |
| $e_{15} = 0$ C/m$^2$ | $e_{24} = 0$ C/m$^2$ | |
| $\varepsilon_{11} = 0$ F/m | $\varepsilon_{22} = 0$ F/m | $\varepsilon_{33} = 0.1062$ nF/m |

The piezoelectric coefficients and dielectric permittivities for which no values were reported in the reference works have been set to zero.
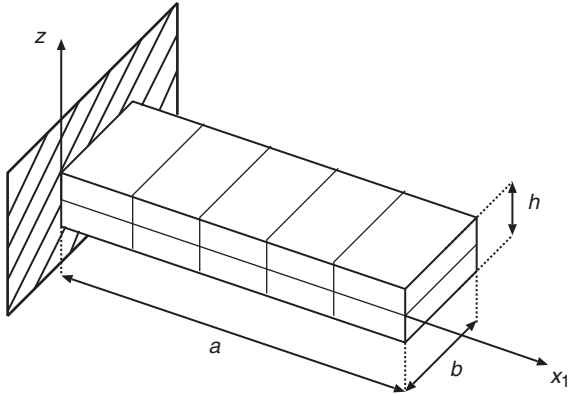


**Figure 5.** Piezoelectric bimorph beam.

**Boundary Conditions:** The cantilevered plate has all mechanical dof blocked on the boundary at $x_1 = 0$.

The boundary conditions for the actuator and sensor configuration are as follows:

- **Actuator case:** Prescribed electric potential at the top and bottom faces of the plate: $\Phi(z = -h/2) = -\Phi(z = +h/2) = 0.5$ V.
- **Sensor case:** As reported by Tan and Vu-Quoc (2005), the tip of the plate is loaded by a vertical force $F = 0.0254371$ N, which corresponds to a deflection of 0.01 m. The bottom face of the plate is grounded, $\phi(z = -h/2) = 0$ V, while the electric potential at the top face is free.

**Mesh:** A regular mesh with five elements is used with $m_{x_1} = 5$, $m_{x_2} = 1$ as depicted in Figure 5. One numerical layer is used for each PVDF ply.

**Results:** For the actuator case, the plate deflection at the mean surface $u_3(z = 0)$ is reported. For the sensor case, the electric potential at the top surface $\Phi(z = h/2)$ is given.

### ACTUATOR CASE

The deflection of the bimorph under the action of an imposed electric field is computed. The numerical results are reported in Table 3 along with the experimental output and the analytical result. The present C7CL8PZ element yields results similar to those found in literature. In general, the predicted tip deflection is about 9% larger than the experimentally measured one. This may be explained by voltage leakage, imperfect bonding, energy dissipation, etc. (Suleman and Venkayya, 1995).

### SENSOR CASE

The electrostatic potential measured at the top surface at various distances from the clamped edge is reported in Table 4 and Figure 6. A good agreement is found with results found in literature. Note that the values of the literature have been extracted from graphical results reported in the cited references. While the element TVQ-2005 has a bilinear interpolation for the electric

**Table 3. Nodal deflection of the bimorph piezoelectric actuator (μm).**

| Distance from clamping (mm) | 20 | 40 | 60 | 80 | 100 |
|---|---|---|---|---|---|
| Experiment (Tzou et al., 1990) | – | – | – | – | 0.315 |
| Analytical (Tzou, 1993) | 0.0138 | 0.0552 | 0.1242 | 0.2208 | 0.3450 |
| ISOP4 | 0.0138 | 0.0552 | 0.1242 | 0.2208 | 0.3450 |
| BN-2001 | 0.0144 | 0.0557 | 0.1240 | 0.2192 | 0.3415 |
| ISOP9 | 0.0137 | 0.0551 | 0.1241 | 0.2207 | 0.3449 |
| TVQ-2005 | 0.0138 | 0.0552 | 0.1242 | 0.2208 | 0.3450 |
| GEXP4 | 0.0138 | 0.0552 | 0.1242 | 0.2208 | 0.3450 |
| C7CL8PZ | 0.0137 | 0.0551 | 0.1241 | 0.2207 | 0.3449 |

potential distribution across the element, the electric potential is constant across the C7CL8PZ and BN-2001 elements (Table 2). For these elements, Table 4 reports two nodal values corresponding to the adjacent elements and a piece-wise constant distribution is obtained along the axis (Figure 6). In reality, the voltage is averaged at the common node between adjacent elements due to conductivity.

## Closed Cylindrical Rings

We consider a problem formulated by Heyliger et al. (1996), which addresses the static response of mechanically loaded circular rings. Two cases are considered, a homogeneous ring made of PZT-4 and a composite ring made of Titanium and PZT-4. A new reference solution is additionally proposed which has been obtained by a 3D FE model calculated by ANSYS.

### HOMOGENEOUS PZT-4 RING
*Geometry*
The circular ring has an inner radius of $R_i = 0.289$ m and a depth of $b = 0.3048$ m, see the notation in Figure 9. Two values for the ring wall thickness are considered, a thin ring with $h = 0.004$ m and a thick ring with $h = 0.04$ m (Heyliger et al., 1996).

*Material*
The PZT-4 has the following properties (Heyliger et al., 1996):

$E_1 = 81.3$ GPa $\quad \nu_{12} = 0.329 \quad G_{12} = 30.6$ GPa

$E_2 = 81.3$ GPa $\quad \nu_{13} = 0.432 \quad G_{13} = 25.6$ GPa

$E_3 = 64.5$ GPa $\quad \nu_{23} = 0.432 \quad G_{23} = 25.6$ GPa

$e_{31} = -5.2$ C/m$^2 \quad e_{32} = -5.2$ C/m$^2 \quad e_{33} = 15.08$ C/m$^2$

$e_{15} = 12.72$ C/m$^2 \quad e_{24} = 12.72$ C/m$^2$

$\epsilon_{11} = 13.06$ nF/m $\quad \epsilon_{22} = 13.06$ nF/m $\quad \epsilon_{33} = 11.51$ nF/m

*Boundary Conditions*
The ring is unsupported and loaded at $\theta = \pm 90°$ by a radial line load $F_{X_1} = 656.17$ N/m. Differently from Heyliger et al. (1996), we consider that both the inner and outer surfaces are grounded (short-circuit condition,

$\phi(z = \pm h/2) = 0$ V) for both the thick and thin ring cases. Due to symmetry, the model can be reduced to one eighth of the ring by applying corresponding symmetry boundary conditions at $\theta = 0°$, $90°$ and $x_2 = b/2$ (the same notation of Figure 9 is employed).

*Mesh*
The symmetric model is discretized with $m_{x_2} = 2$ elements along the cylinder axis $x_2$ and with $m_{x_1} = 16$ elements along the hoop axis $x_1$ (Figure 9). Additionally, the piezoelectric ring will be subdivided into various numerical layers, denoted $m_z$, in order to refine the description of the electrostatic potential.

*Results*
The distributions along the circumferential direction of the electric potential $\phi(\theta)$ and of the radial deflection $u_z(\theta)$ are given. The values are taken at the center of the ring, $x_2 = b/2$, and at the middle surface $z = 0$ (Figure 9).

We compare the results of the present C7CL8PZ element with the reference solution issued from a 3D FE calculation of ANSYS. The proper mesh densities to be used for the 3D FE solutions have been obtained from preliminary convergence studies like the one reported in Table 5.
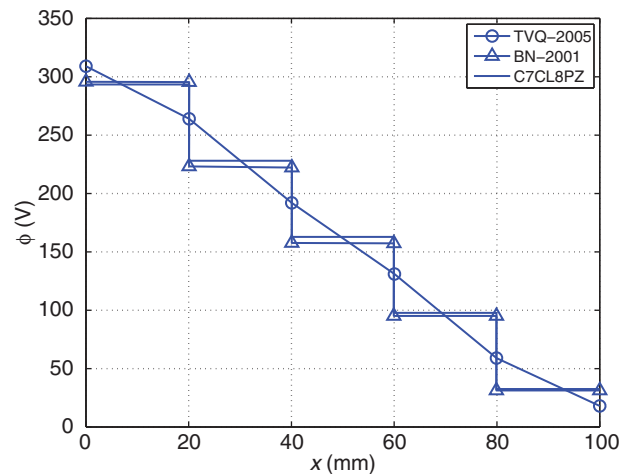


**Figure 6.** *Distribution along the axis of the induced potential at the top surface of the PVDF bimorph.*

**Table 4. Induced electrostatic potential at the top surface of the bimorph piezoelectric plate (V).**

| Distance from clamping (mm) | 0 | 20 | 40 | 60 | 80 | 100 |
|---|---|---|---|---|---|---|
| TVQ-2005 | 309 | 264 | 192 | 131 | 59 | 18 |
| BN-2001 | 297 | 224 | 157 | 93 | 30 | |
| | | 297 | 224 | 157 | 93 | 30 |
| C7CL8PZ | 293 | 228 | 163 | 98 | 32 | |
| | | 293 | 228 | 163 | 98 | 32 |

**Table 5. Convergence study for the 3D FE computation of the thick PZT-4 ring: $u_z(\theta = 0°)$.**

| Refinement along $x_1$: $m_{x_2} = 20$; $m_z = 16$ | | | | | |
|---|---|---|---|---|---|
| $m_{x_1}$ | 10 | 20 | 30 | 40 | 60 |
| Error (%) | 2.2 | 2.2 | 0.1 | 0.0 | 0.0 |
| Refinement along $x_2$: $m_{x_1} = 60$; $m_z = 16$ | | | | | |
| $m_{x_2}$ | – | 5 | 10 | 15 | 20 |
| Error (%) | – | 1.2 | 0.05 | 0.01 | 0.0 |
| Refinement along $z$: $m_{x_1} = 60$; $m_{x_2} = 20$ | | | | | |
| $m_z$ | – | 2 | 4 | 8 | 16 |
| Error (%) | – | 0.2 | 0.07 | 0.01 | 0.0 |

A convergence analysis is presented in Table 6 for the present shell element C7CL8PZ. The radial displacements $u_z$ at $\theta = 0°$ and $\theta = 90°$ are analyzed. We vary both the in-plane discretization and the number of numerical layers into which the piezoelectric material is subdivided along the thickness direction. Table 6 shows that the element has a high convergence velocity

**Table 6. In-plane convergence study for the present shell element, thin PZT-4 ring: percentage error with respect to 3D FE solution for $u_z(\theta=0°)$ and $u_z(\theta=90°)$.**

|  | $m_{x_2} \times m_{x_1}$; $m_z = 8$ | | | | |
|---|---|---|---|---|---|
|  | $2 \times 2$ | $2 \times 4$ | $2 \times 8$ | $2 \times 16$ | $2 \times 24$ |
| Error (%) for $u_z(0°)$ | 7 | 2.5 | 1 | 0.7 | 0.6 |
| Error (%) for $u_z(90°)$ | 6.7 | 2.1 | 0.9 | 0.6 | 0.6 |

**Table 7. Convergence study of the present shell element: influence of the number of numerical layers $m_z$ on the radial deflections $u_z(\theta=0°)$ and $u_z(\theta=90°)$ and the percentage errors with respect to the 3D FE solution ($m_{x_1}=16$, $m_{x_2}=2$).**

| | Thin homogeneous PZT-4 ring | | | |
|---|---|---|---|---|
| $m_z$ | $u_z(\theta=0°)$ | Error (%) | $u_z(\theta=90°)$ | Error (%) |
| 1 | 0.50519E-02 | 16 | −0.46390E-02 | 16 |
| 2 | 0.45033E-02 | 4 | −0.41353E-02 | 4 |
| 4 | 0.43870E-02 | 1.2 | −0.40285E-02 | 1.2 |
| 8 | 0.43590E-02 | 0.6 | −0.40028E-02 | 0.6 |
| 3D FEM | 0.43320E-02 | | −0.39788E-02 | |
| 1 | 0.64665E-05 | 13 | −0.58305E-05 | 11 |
| 2 | 0.59253E-05 | 4 | −0.53397E-05 | 4 |
| 4 | 0.58136E-05 | 2 | −0.52386E-05 | 1.8 |
| 8 | 0.57869E-05 | 1.7 | −0.52144E-05 | 1.3 |
| 3D FEM | 0.56899E-05 | | −0.51435E-05 | |

toward the reference solution issued from the 3D FE computation even for a thin ring. Based on these results, the mesh density with $m_{x_1} = 16$ and $m_{x_2} = 2$ will be taken for the following computations.

The influence of the number of numerical layers $m_z$ is assessed in Table 7 for the thin and thick PZT-4 ring. Convergence toward the 3D FE solution is recognized. A noticeable influence of $m_z$ is remarked, which confirms the important role played by the induced electric potential by taking $m_z = 1$, the linear approximation for the electric potential $\phi$ neglects the additional stiffness due to the direct piezoelectric effect and leads to errors greater than 10%. Note that this error is greater for the thin piezoelectric ring. Upon increasing $m_z$, a piece-wise linear refinement of the radial distribution of $\phi$ allows to take into account the piezoelectric stiffening effect. In the following, $m_z = 4$ numerical layers will be employed for the piezoelectric layer, which bounds the error to about 2%.

Finally, the variation along the circumferential direction of the radial deflection $u_z$ and of the electric potential $\phi$ at the mid-surface are reported in Figures 7 and 8, respectively. An excellent agreement is found between the results of the present shell element and the reference 3D FE computation for both the thin and the thick case. Note that the electric potential remains constant across the present shell element.

## COMPOSITE TITANIUM/PZT-4 RING
### Geometry

A circular cylindrical ring is considered that is made of an inner Titanium layer with an attached continuous PZT-4 layer. The inner radius is fixed at $R_i = 0.289$ m, the depth of the ring is $b = 0.3048$ m and the total thickness of the composite ring is $h = 0.04$ m, where the thickness of the Titanium and of the PZT-4 layers are
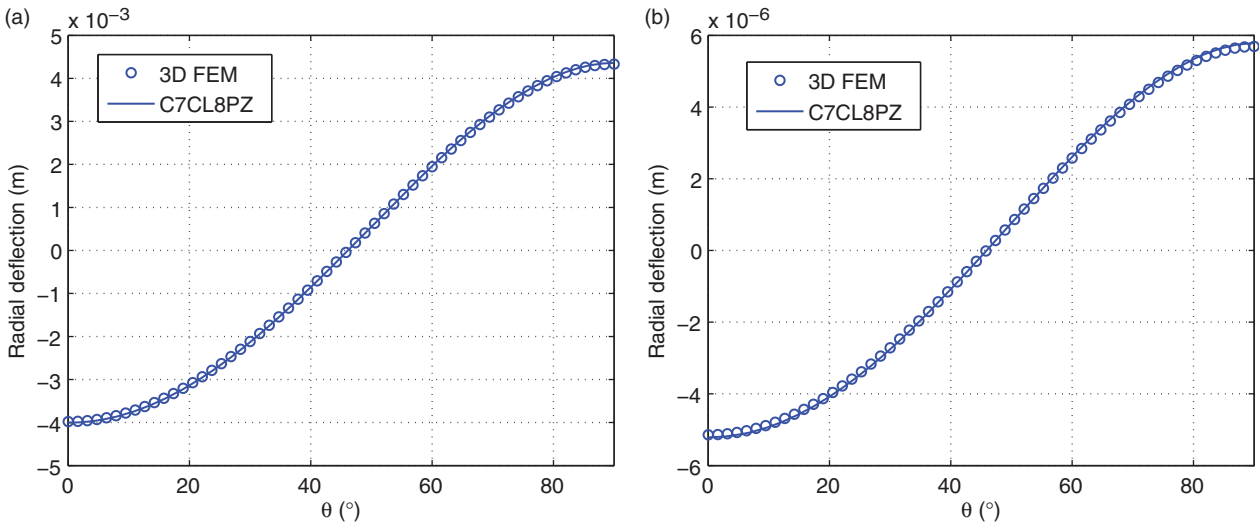


**Figure 7.** Distributions of the radial displacement $u_z(\theta)$ for the thin (left) and thick (right) PZT-4 ring.

$h_T = 0.03$ m and $h_P = 0.01$ m, respectively (Heyliger et al., 1996). For further convenience, we identify the location of the interface between the Titanium and the PZT-4 plies as $z_I = -h/2 + h_T$ and the location of the mid-surface of the PZT-4 ply as $z_P = z_I + h_P/2 = h/2 - h_P/2$. The geometry is depicted in Figure 9 along with the used coordinate axes.

*Material*

The material properties for the PZT-4 coincide with those listed in the previous section, those for the isotropic Titanium layer read (Heyliger et al., 1996):

| | | |
|---|---|---|
| $E_1 = 114$ GPa | $\nu_{12} = 0.3$ | $G_{12} = 43.8$ GPa |
| $E_2 = 114$ GPa | $\nu_{13} = 0.3$ | $G_{13} = 43.8$ GPa |
| $E_3 = 114$ GPa | $\nu_{23} = 0.3$ | $G_{23} = 43.8$ GPa |
| $e_{31} = 0$ C/m² | $e_{32} = 0$ C/m² | $e_{33} = 0$ C/m² |
| $e_{15} = 0$ C/m² | $e_{24} = 0$ C/m² | |
| $\varepsilon_{11} = 13.06$ nF/m | $\varepsilon_{22} = 13.06$ nF/m | $\varepsilon_{33} = 13.06$ nF/m |

*Boundary Conditions*

The cylindrical ring is unsupported and loaded at $\theta = \pm 90°$ by a radial line load $F_{X_1} = 656.17$ N/m. The interface between the perfectly bonded Titanium and PZT-4 layers is grounded, $\phi(z = z_I) = 0$, while the electric potential of the outer surface of the piezoelectric layer $\phi(z = h/2)$ is let free (Heyliger et al., 1996). Symmetry is exploited by modeling only one eighth of the ring upon application of corresponding symmetry conditions at $\theta = 0°$, $90°$ and at $x_2 = b/2$.

*Mesh*

The symmetric model is discretized with $m_{x_1} = 24$ elements along the circumferential direction and $m_{x_2} = 2$ elements along the axis of the cylinder.

*Results*

We report the circumferential distributions of the electric potential $\phi(\theta)$ and of the radial displacement $u_z(\theta)$ taken at the center of the ring ($x_2 = b/2$). The values of the radial displacement are taken at the mid-surface of the ring $z = 0$, while those of the electric potential are taken at the middle surface of the piezoelectric ply, $z = z_P$, and at the outer surface $z = h/2$.

A preliminary convergence analysis is proposed in order to assess the role of the number $m_z$ of numerical layers into which the PZT-4 ply is subdivided. Table 8 reports the radial displacements at $\theta = 0°$ and $\theta = 90°$ for different values of $m_z$. The reference values have been provided by a 3D FE solution of ANSYS. The employed mesh for the 3D solution is $m_{x_1} \times m_{x_2} \times m_z = 60 \times 20 \times 16$. In contrast to the homogeneous short-circuited PZT-4 ring discussed in the previous section, only a marginal influence of $m_z$ can be appreciated with differences of less than 1%. This completely different behavior is attributed to the different electrical boundary
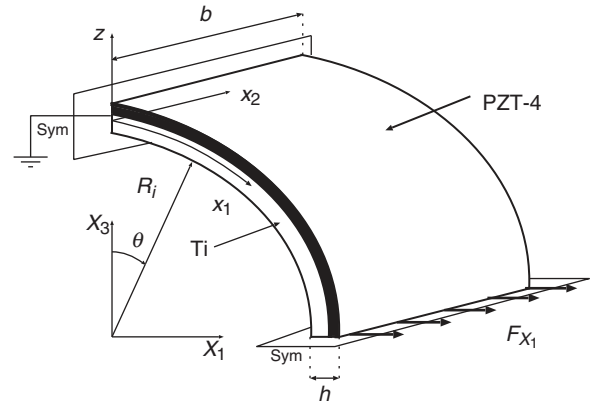


**Figure 9.** *Quarter model of the composite Ti/PZT-4 cylindrical ring: geometry and loading.*
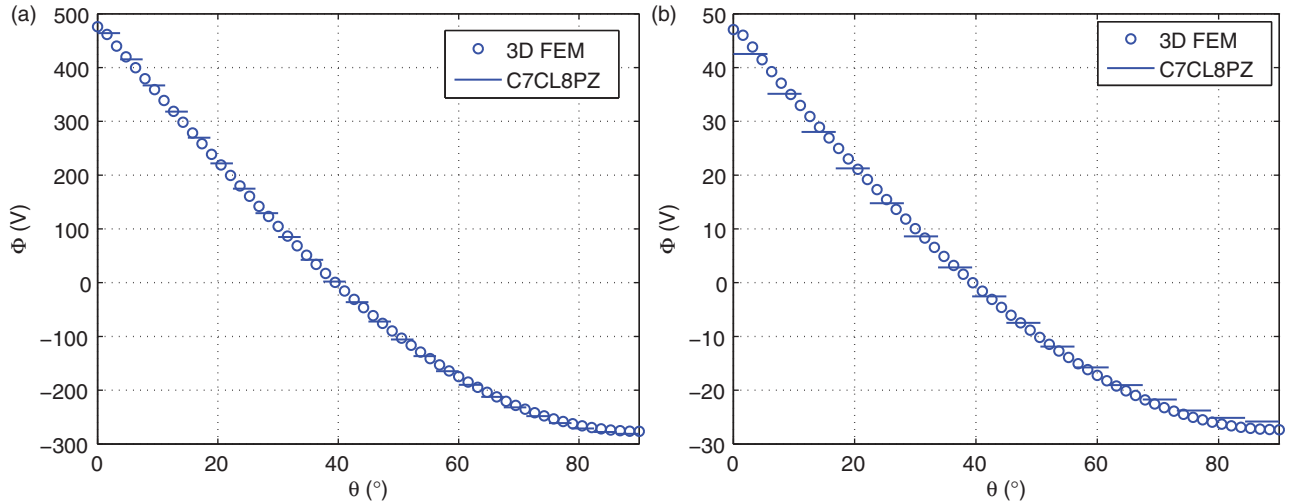


**Figure 8.** *Distributions of the electric potential $\phi(\theta)$ for the thin (left) and thick (right) PZT-4 ring.*

conditions. In fact, an induced electric field can be constructed by a non-zero value of the electric potential at the outer surface, which can be readily obtained by a linear distribution of the electric potential.

**Table 8. Convergence study of the present shell element: influence of the number of numerical layers $m_z$ on the radial deflection at $\theta=0°$ and $\theta=90°$ and the percentage errors with respect to the 3D FE solution.**

| | Thick composite Ti/PZT-4 ring | | | |
|---|---|---|---|---|
| $m_z$ | $u_z(0°)$ | Error (%) | $u_z(90°)$ | Error (%) |
| 1 | 0.50433E-05 | 0.79 | −0.45595E-05 | 0.64 |
| 2 | 0.50374E-05 | 0.67 | −0.45541E-05 | 0.52 |
| 4 | 0.50360E-05 | 0.64 | −0.45528E-05 | 0.50 |
| 3D FEM | 0.50036E-05 | | −0.45301E-05 | |



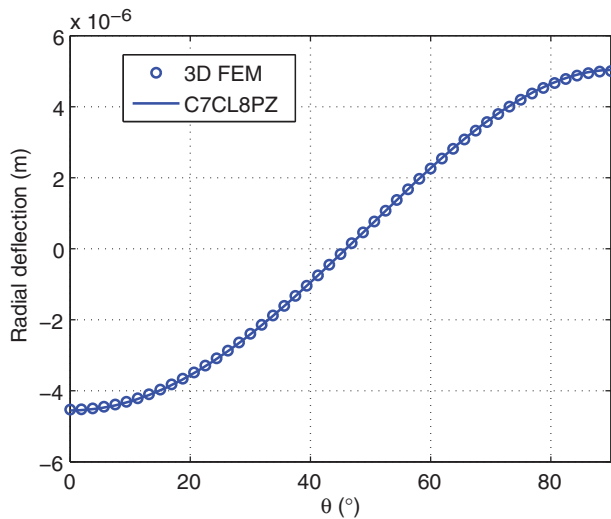**Figure 10.** *Distribution of the radial displacement $u_z(\theta)$ for the mechanically loaded Ti/PZT-4 composite cylindrical ring.*

The circumferential distributions of the radial displacement $u_z(\theta, z=0)$ and of the electrostatic potential $\phi(\theta, z=z_P)$ and $\phi(\theta, z=h/2)$ are illustrated in Figures 10 and 11, respectively. An excellent agreement is found between the results of the present shell element and those issued from the 3D FE solution.

**Composite Cylindrical Shell Panels**

The last examples shall validate our C7CL8PZ element with respect to applications involving composite layups made of orthotropic elastic materials and piezoelectric plies. Two case studies are addressed, a simply supported orthotropic panel and a cantilever panel with bending–twisting elastic coupling.

*SIMPLY-SUPPORTED COMPOSITE CYLINDRICAL SHELL PANEL*

This example has been formulated by Saravanos (1997) for validating his 8-node quadrilateral element S-1997. It consists of a simply supported 90° cylindrical shell panel made of the symmetric stack $[0/90]_s$ of graphite–epoxy (Gr–Ep) composite. A continuous piezoelectric actuator is either embedded into the stack or attached to the inner or outer surface of the panel. Figure 12 illustrates the configuration with the actuator placed at the inner (bottom) surface of the composite stack.

*Geometry*

The 90° cylindrical panel has a thickness of $h=2$ mm and a mid-surface radius $R=200$ mm $(R/h=100)$. The panel is square with $b=\pi R/2$ (Figure 12). Each composite Gr–Ep ply has a thickness $h_C=0.375$ mm and the thickness of the piezoelectric actuator is $h_P=0.5$ mm. Three configurations are considered for the laminated actuator: [p/0/90/90/0], [0/90/p/90/0], and [0/90/90/0/p], where the placement of the
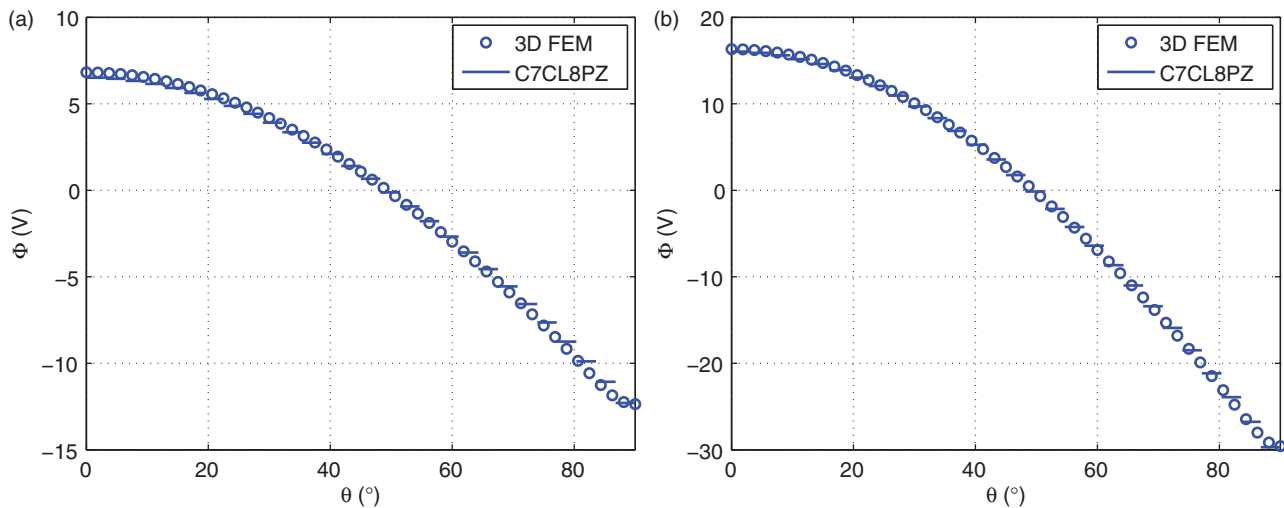


**Figure 11.** *Distributions of the electric potential $\phi(\theta)$ at the middle surface of the PZT-4 ply ($z=z_P$, left) and at the outer surface ($z=h/2$, right) for the mechanically loaded Ti/PZT-4 composite cylindrical ring.*

piezoelectric actuator ($p$) is at the inner, middle, and outer surface, respectively.

*Material*

Both the elastic Gr–Ep composite and the piezoelectric actuator are assumed to be transversely isotropic. The following properties are assumed for the Gr–Ep composite ply (Saravanos, 1997; Benjeddou et al., 2002):

| | | |
|---|---|---|
| $E_1 = 132.4\,\text{GPa}$ | $\nu_{12} = 0.24$ | $G_{12} = 5.6\,\text{GPa}$ |
| $E_2 = 10.8\,\text{GPa}$ | $\nu_{13} = 0.24$ | $G_{13} = 5.6\,\text{GPa}$ |
| $E_3 = 10.8\,\text{GPa}$ | $\nu_{23} = 0.49$ | $G_{23} = 3.6\,\text{GPa}$ |
| $e_{31} = 0\,\text{C/m}^2$ | $e_{32} = 0\,\text{C/m}^2$ | $e_{33} = 0\,\text{C/m}^2$ |
| $e_{15} = 0\,\text{C/m}^2$ | $e_{24} = 0\,\text{C/m}^2$ | |
| $\epsilon_{11} = 3.5\,\epsilon_0$ | $\epsilon_{22} = 3\,\epsilon_0$ | $\epsilon_{33} = 3\,\epsilon_0$ |

where $\epsilon_0 = 8.85 \times 10^{-12}\,\text{F/m}$ is the vacuum permittivity constant. The actuator consists of the piezoceramic material PZT-4 and has the following characteristics (Saravanos, 1997; Benjeddou et al., 2002):

| | | |
|---|---|---|
| $E_1 = 81.3\,\text{GPa}$ | $\nu_{12} = 0.33$ | $G_{12} = 30.6\,\text{GPa}$ |
| $E_2 = 81.3\,\text{GPa}$ | $\nu_{13} = 0.43$ | $G_{13} = 25.6\,\text{GPa}$ |
| $E_3 = 64.5\,\text{GPa}$ | $\nu_{23} = 0.43$ | $G_{23} = 25.6\,\text{GPa}$ |
| $e_{31} = -5.2\,\text{C/m}^2$ | $e_{32} = -5.2\,\text{C/m}^2$ | $e_{33} = 15.08\,\text{C/m}^2$ |
| $e_{15} = 12.72\,\text{C/m}^2$ | $e_{24} = 12.72\,\text{C/m}^2$ | |
| $\epsilon_{11} = 1475\,\epsilon_0$ | $\epsilon_{22} = 1475\,\epsilon_0$ | $\epsilon_{33} = 1300\,\epsilon_0$ |

*Boundary Conditions*

All edges of the cylindrical shell panel are simply supported: $v_{x_2} = v_z = 0$ at $x_1 = 0$, $\pi/2$ and $v_{x_1} = v_z = 0$ at $x_2 = 0$, $b$. A uniform electric field $E_z = -400\,\text{kV m}^{-1}$ is imposed in the PZT actuator through the following electric potentials at the bottom and top electrodes: $\phi_{bot} = 0$, $\phi_{top} = 200\,\text{V}$.
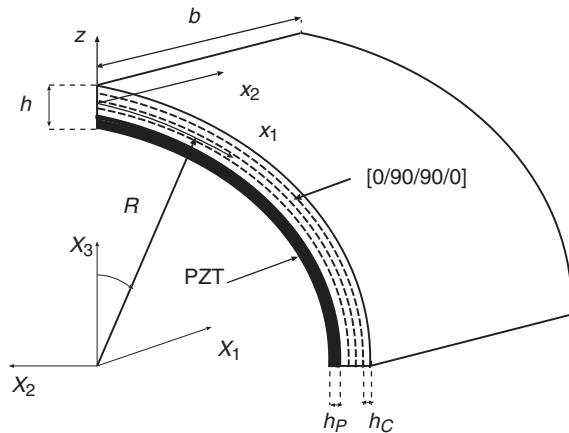
*Mesh*

The shell reference surface has been discretized with $m_{x_2} = 4$ elements along the cylinder axis $x_2$ and $m_{x_1} = 15$ elements in the circumferential direction (hoop axis $x_1$).

*Results*

The non-dimensional radial deflection $u_z/h$ is reported at the mid-surface along the axial mid-span of the panel (i.e., at points located at $x_2 = b/2$, $z = 0$, see Figure 12).

Figure 13 illustrates the distribution of the non-dimensional radial deflection $u_z/h$ along the axial mid-span of the shell for the three configurations ([p/0/90/90/0], [0/90/p/90/0], and [0/90/90/0/p]). The results of the present element are compared with those of Saravanos (1997) and Balamurugan and Narayanan (2008). Additionally, we report the results issued from a 3D FE computation made with ANSYS. The employed mesh density for the 3D FE computation is $m_{x_1} = 80$, $m_{x_2} = 40$, and $m_z = 10$.

A good agreement is found between all approaches. The comparison between the three configurations shows that the position of the actuator in the composite stack has an important influence on the deformed shape. Note that the solid shell element BN-2008 retains the induced electric field by a quadratic approximation for the electric potential. As already recognized by Balamurugan and Narayanan (2008), their element appears to be the stiffest one.

## CANTILEVER CYLINDRICAL SHELL

A clamped composite shell panel with attached piezoceramic actuators is considered as proposed by Kioua and Mirza (2000). The piezoelectric composite shell has the symmetric stacking $[p/30/30/0]_s$ and shows a bending–twisting coupling under the action of the actuators. The data for the case study is summarized in the following.



**Figure 12.** *The 90° cylindrical panel [p/0/90/90/0]: a composite elastic laminate with a PZT actuator (p) attached to the inner (bottom) surface.*
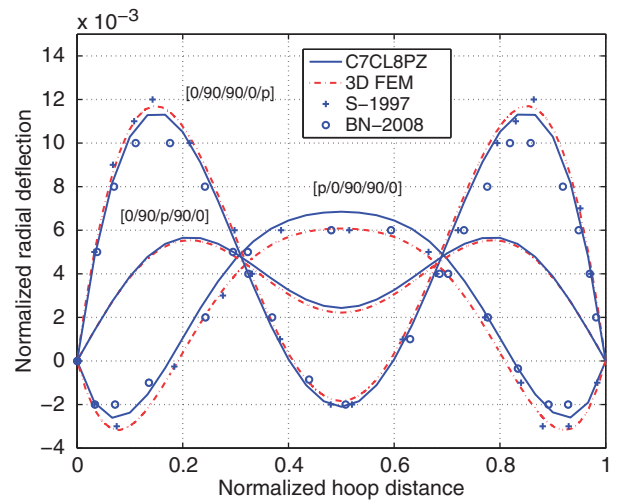


**Figure 13.** *Simply supported 90° composite shell panel: effect of thickness location of the actuator.*

## Geometry

The cylindrical shell illustrated in Figure 14 is considered. It has square in-plane dimensions $a = b = 0.254\,\text{m}$ and the mid-surface curvature radius $R$ is varied within the range of validity of shallow shell approximations between $R/b = 10$ and $R/b = 100$ (Kioua and Mirza, 2000). Each composite Gr–Ep ply has a thickness of $h_C = 0.138\,\text{mm}$, each piezoelectric actuator has the thickness $h_P = 0.254\,\text{mm}$ and the total thickness of the symmetric stack $[p/30/30/0]_s$ is $h = 1.336\,\text{mm}$.

## Material

The material data reported by Kioua and Mirza (2000) were limited to the in-plane properties and no electric permittivities were indicated. In this study, the data set has been completed by referring to similar material properties available in literature. The material properties for Gr–Ep given by Kioua and Mirza (2000) are close to those of the T300/976 composite, for which the complete data set has been provided by Benjeddou et al. (2002). The following data are used in this study:

| | | |
|---|---|---|
| $E_1 = 150\,\text{GPa}$ | $\nu_{12} = 0.3$ | $G_{12} = 7.1\,\text{GPa}$ |
| $E_2 = 9\,\text{GPa}$ | $\nu_{13} = 0.3$ | $G_{13} = 7.1\,\text{GPa}$ |
| $E_3 = 9\,\text{GPa}$ | $\nu_{23} = 0.49$ | $G_{23} = 3\,\text{GPa}$ |
| $e_{31} = 0\,\text{C/m}^2$ | $e_{32} = 0\,\text{C/m}^2$ | $e_{33} = 0\,\text{C/m}^2$ |
| $e_{15} = 0\,\text{C/m}^2$ | $e_{24} = 0\,\text{C/m}^2$ | |
| $\epsilon_{11} = 0.031\,\text{nF/m}$ | $\epsilon_{22} = 0.027\,\text{nF/m}$ | $\epsilon_{33} = 0.027\,\text{nF/m}$ |

The actuators are two PZT G1195 plies with opposite polarization directions. Unfortunately, the elastic stiffness data for the PZT G1195 reported by Benjeddou et al. (2002) do not agree with those used in the original work of Kioua and Mirza (2000). A piezoelectric material with elastic properties similar to those given by Kioua and Mirza (2000) has been found in the work of Lee 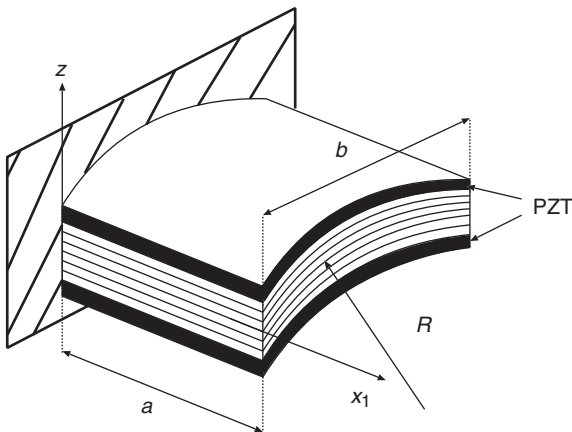and Saravanos (1999), where reference is made to an isotropic piezoceramic. As a result, the following isotropic properties are employed in this study:

| | | |
|---|---|---|
| $E_1 = 63\,\text{GPa}$ | $\nu_{12} = 0.3$ | $G_{12} = 24.2\,\text{GPa}$ |
| $E_2 = 63\,\text{GPa}$ | $\nu_{13} = 0.3$ | $G_{13} = 24.2\,\text{GPa}$ |
| $E_3 = 63\,\text{GPa}$ | $\nu_{23} = 0.3$ | $G_{23} = 24.2\,\text{GPa}$ |
| $e_{31} = 22.86\,\text{C/m}^2$ | $e_{32} = 22.86\,\text{C/m}^2$ | $e_{33} = 0\,\text{C/m}^2$ |
| $e_{15} = 0\,\text{C/m}^2$ | $e_{24} = 0\,\text{C/m}^2$ | |
| $\epsilon_{11} = 15.05\,\text{nF/m}$ | $\epsilon_{22} = 15.05\,\text{nF/m}$ | $\epsilon_{33} = 15.05\,\text{nF/m}$ |

## Boundary Conditions

The shell is clamped at one of its curved edges. An electric field is induced in the piezoceramic actuators by applying an electric potential of $\phi = 100\,\text{V}$ at the outer electrodes while the inner surfaces are grounded.

## Mesh

A regular mesh with eight elements per edge is used.

## Results

The magnified mid-span tip deflection $10^3\,u_3(a, b/2)$ is reported along with a magnified measure of the twist. The twist is computed as the ratio between the difference of the deflections at the tip corners and the width $b$: $10^3\,[u_3(a, b) - u_3(a, 0)]/b$.

The results are reported in Figure 15 by plotting the evolution of the tip deflection and twist with respect to the curvature ratio $R/b$ of the panel. Present results are compared with those obtained with the finite shell elements ISOP9 (Lee et al., 2003) and GEXP4 (Kulikov and Plotnikova, 2008), see also Table 2. A perfect agreement between the different element formulations can be seen, which validates the present element formulation with respect to its capability of modeling piezoelectric composite shells.
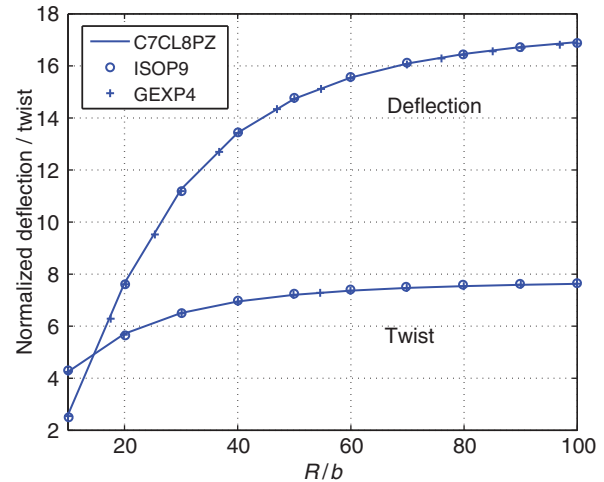


**Figure 14.** Cantilever composite cylindrical shell with attached piezoelectric actuators.



**Figure 15.** Actuated cantilever composite shell: magnified deflection ($10^3\,u_3(a, b/2)/b$) and twist ($10^3\,[u_3(a, b) - u_3(a, 0)]/b$) for various curvature ratios $R/b$.

## CONCLUSION

This article has presented a new and simple finite shell element for multilayered panels including piezoelectric actuators and/or sensors. The shell model consists of the classical Reissner–Mindlin kinematics with an additional quadratic thickness stretch term that permits to retain the full 3D constitutive law without Poisson locking problems. A layer-wise linear assumption has been used for the electrostatic potential. The FE approximations of the employed 8-node element have been detailed out along with an efficient technique to avoid transverse shear and membrane locking. The electric potential is constant over the elementary domain, which ensures efficiency and a direct satisfaction of the equipotentiality condition on the patch electrodes. The element has been validated through various linear static case studies for which a rather large number of results were provided in literature. Flat plates as well as open and closed shells have been considered that were made up of homogeneous or laminated materials. New reference solutions have been provided by means of 3D FEM computations with a commercial software.

In general, a very good agreement has been found between the reference solutions and the results of the proposed shell element. The capability to properly represent the piezoelectric coupling in both actuator and sensor cases has been demonstrated. In particular, the electric field induced by the direct piezoelectric effect could be well captured upon subdividing the piezoelectric ply into several numerical layers. Based on the promising results obtained for linear static applications, future works should address the extension of the proposed shell element to linear dynamics and its application to active control and optimization problems.

## REFERENCES

ANSI/IEEE Std 176-1987. 1987. *IEEE Standard on Piezoelectricity*, American National Standard Institute, New York, NY.

Balamurugan, V. and Narayanan, S. 2001. "Shell Finite Element for Smart Piezoelectric Composite Plate/Shell Structures and its Application to the Study of Active Vibration Control," *Finite Elements in Analysis and Design*, 37:713–738.

Balamurugan, V. and Narayanan, S. 2008. "A Piezolaminated Composite Degenerated Shell Finite Element for Active Control of Structures with Distributed Piezosensors and Actuators," *Smart Materials and Structures*, 17:035031.1–18.

Ballhause, D., D'Ottavio, M., Kröplin, B. and Carrera, E. 2005. "A Unified Formulation to Assess Multilayered Theories for Piezoelectric Plates," *Computers & Structures*, 83:1217–1235.

Benjeddou, A. 2000. "Advances in Piezoelectric Finite Element Modeling of Adaptive Structural Elements: A Survey," *Computers & Structures*, 76:347–363.

Benjeddou, A., Deu, J.F. and Letombe, S. 2002. "Free Vibrations of Simply-supported Piezoelectric Adaptive Plates: An Exact Sandwich Formulation," *Thin-Walled Structures*, 40:573–593.

Benjeddou, A., Trindade, M.A. and Ohayon, R. 2000. "Piezoelectric Actuation Mechanisms for Intelligent Sandwich Structures," *Smart Materials and Structures*, 9:328–335.

Bisegna, P. and Maceri, F. 1996. "An Exact Three-dimensional Solution for Simply Supported Rectangular Piezoelectric Plates," *Journal of Applied Mechanics*, 63:628–638.

Carrera, E., Boscolo, M. and Robaldo, A. 2007. "Hierarchic Multilayered Plate Elements for Coupled Multifield Problems of Piezoelectric Adaptive Structures: Formulation and Numerical Assessment," *Archives of Computational Methods in Engineering*, 14:383–430.

Carrera, E. and Brischetto, S. 2007. "Piezoelectric Shells Theories with 'a priori' Continuous Transverse Electro-mechanical Variables," *Journal of Mechanics of Materials and Structures*, 2:377–399.

Carrera, E. and Brischetto, S. 2008. "Analysis of Thickness Locking in Classical, Refined and Mixed Theories for Layered Shells," *Composite Structures*, 85:83–90.

Chevallier, G., Ghorbel, S. and Benjeddou, A. 2008. "A Benchmark for Free Vibration and Effective Coupling of Thick Piezoelectric Smart Structures," *Smart Materials and Structures*, 17:065007.

Cho, M. and Oh, J. 2003. "Higher Order Zig-Zag Plate Theory Under Thermo-electric-mechanical Loads Combined," *Composites Part B: Engineering*, 34:67–82.

Chopra, I. 2002. "Review of State of Art of Smart Structures and Integrated Systems," *AIAA Journal*, 40:2145–2187.

D'Ottavio, M. and Polit, O. 2009. "Sensitivity Analysis of Thickness Assumptions for Piezoelectric Plate Models," *Journal of Intelligent Material Systems and Structures*, 20:1815–1834.

Fernandes, A. and Pouget, J. 2003. "Analytical and Numerical Approaches to Piezoelectric Bimorphs," *International Journal of Solids and Structures*, 40:4331–4352.

Gibson, R.F. 2010. "A Review of Recent Research on Mechanics of Multifunctional Composite Materials and Structures," *Composite Structures*, 92:2793–2810.

Gopinathan, S.V., Varadan, V.V. and Varadan, V.K. 2000. "A Review and Critique of Theories for Piezoelectric Laminates," *Smart Materials and Structures*, 9:24–48.

Heyliger, P.R., Pei, K.C. and Saravanos, D.A. 1996. "Layerwise Mechanics and Finite Element Model for Laminated Piezoelectric Shells," *AIAA Journal*, 34:2353–2360.

Kioua, H. and Mirza, S. 2000. "Piezoelectric Induced Bending and Twisting of Laminated Composite Shallow Shells," *Smart Materials and Structures*, 9:476–484.

Klinkel, S. and Wagner, W. 2006. "A Geometrically Non-linear Piezoelectric Solid Shell Element Based on a Mixed Multi-field Variational Formulation," *International Journal for Numerical Methods in Engineering*, 65:349–382.

Klinkel, S. and Wagner, W. 2008. "A Piezoelectric Solid Shell Element Based on a Mixed Variational Formulation for Geometrically Linear and Nonlinear Applications," *Computers & Structures*, 86:38–46.

Kögl, M. and Bucalem, M.L. 2005. "Analysis of Smart Laminates Using Piezoelectric MITC Plate and Shell Elements," *Computers & Structures*, 83:1153–1163.

Kulikov, G.M. and Plotnikova, S.V. 2008. "Geometrically Exact Four-node Piezoelectric Solid-shell Element," *Mechanics of Advanced Materials and Structures*, 15:199–207.

Kulkarni, S.A. and Bajoria, K.M. 2003. "Finite Element Modeling of Smart Plates/Shells Using Higher Order Shear Deformation Theory," *Composite Structures*, 62:41–50.

Lammering, R. 1991. "The Application of a Finite Shell Element for Composites Containing Piezoelectric Polymers in Vibration Control," *Computers & Structures*, 41:1101–1109.

Lammering, R. and Mesecke-Rischmann, S. 2003. "Multi-field Variational Formulations and Related Finite Elements for Piezoelectric Shells," *Smart Materials and Structures*, 12:904–913.

Lee, S., Goo, N.S., Park, H.C., Yoon, K.J. and Cho, C. 2003. "A Nine-node Assumed Strain Shell Element for Analysis of a Coupled Electro-mechanical System," *Smart Materials and Structures*, 12:355–362.

Lee, H.-J. and Saravanos, D.A. 1999. "A Mixed Multi-Field Finite Element Formulation for Thermopiezoelectric Composite Shells," Technical Report TM-1999-000000, NASA.

Marinkovich, D., Köppe, H. and Gabbert, U. 2006. "Numerically Efficient Finite Element Formulation for Modelling Active Composite Laminates," *Mechanics of Advanced Materials and Structures*, 13:379–392.

Mitchell, J.A. and Reddy, J.N. 1995. "A Refined Hybrid Plate Theory for Composite Laminates with Piezoelectric Laminae," *International Journal of Solids and Structures*, 32:2345–2367.

Pablo, F., Bruant, I. and Polit, O. 2009. "Use of Classical Plate Finite Elements for the Analysis of Electroactive Composite Plates. Numerical Validations," *Journal of Intelligent Material Systems and Structures*, 20:1861–1874.

Polit, O. and Bruant, I. 2006. "Electric Potential Approximations for an Eight Node Plate Finite Element," *Computers & Structures*, 84:1480–1493.

Polit, O. and Touratier, M. 1999. "A c⁰eight Node Finite Element Based on the Semi-thick Doubly Curved Shell Theory: Comparison with the Degenerated Approach," *Revue Européenne des Éléments Finis*, 8:111–134.

Polit, O., Touratier, M. and Lory, P. 1994. "A New Eight-node Quadrilateral Shear-bending Plate Finite Element," *International Journal for Numerical Methods in Engineering*, 37:387–411.

Robbins Jr, D.H. and Chopra, I. 2006. "The Effect of Laminate Kinematic Assumptions on the Global Response of Actuated Plates," *Journal of Intelligent Material Systems and Structures*, 17:273–299.

Rogacheva, N.N. 1994. *The Theory of Piezoelectric Shells and Plates*, CRC Press, Boca Raton, FL.

Saravanos, D.A. 1997. "Mixed-field Laminate Theory and Finite Element for Smart Piezoelectric Composite Shell Structures," *AIAA Journal*, 35:1327–1333.

Saravanos, D.A. and Heyliger, P.R. 1999. "Mechanics and Computational Models for Laminated Piezoelectric Beams, Plates and Shells," *Applied Mechanics Reviews*, 52:305–319.

Suleman, A. and Venkayya, V.B. 1995. "A Simple Finite Element Formulation for a Laminated Composite Plate with Piezoelectric Layers," *Journal of Intelligent Material Systems and Structures*, 6:776–782.

Sze, K.Y., Yang, X.M. and Fan, H. 2004. "Electric Assumptions for Piezoelectric Laminate Analysis," *International Journal of Solids and Structures*, 41:2363–2382.

Sze, K.Y., Yao, L.E. and Yi, S. 2000. "A Hybrid Stress ANS Solid-shell Element and its Generalization for Smart Structure Modelling. Part II-Smart Structure Modelling," *International Journal for Numerical Methods in Engineering*, 48:565–582.

Tan, X.G. and Vu-Quoc, L. 2005. "Optimal Solid Shell Element for Large Deformable Composite Structures with Piezoelectric Layers and Active Vibration Control," *International Journal for Numerical Methods in Engineering*, 64:1981–2013.

Tiersten, H.F. 1969. *Linear Piezoelectric Plate Vibrations*, Plenum, New York, NY.

Tzou, H.S. 1993. *Piezoelectric Shells: Distributed Sensing and Control of Continua*, Kluwer-Academic, Dordrecht, The Netherlands.

Tzou, H.S., Tseng, C.I. and Wan, G.C. 1990. "Distributed Structural Dynamics Control of Flexible Manipulators—II. Distributed Sensor and Active Electromechanical Actuator," *Computers & Structures*, 35:679–687.

Varelis, D. and Saravanos, D.A. 2006. "Coupled Mechanics and Finite Element for Non-linear Laminated Piezoelectric Shallow Shells Undergoing Large Displacements and Rotations," *International Journal for Numerical Methods in Engineering*, 66:1211–1233.

Yao, L.-Q. and Lu, L. 2005. "An Electric Node Concept for Solid-shell Elements for Laminate Composite Piezoelectric Structures," *Journal of Applied Mechanics*, 72:35–43.

Zemčík, R., Rolfes, R., Rose, M. and Tessmer, J. 2007. "High-Performance Four-node Shell Element with Piezoelectric Coupling for the Analysis of Smart Laminated Structures," *International Journal for Numerical Methods in Engineering*, 70:934–961.

Zheng, S., Wang, X. and Chen, W. 2004. "The Formulation of a Refined Hybrid Enhanced Assumed Strain Solid Shell Element and Its Application to Model Smart Structures Containing Distributed Piezoelectric Sensors/Actuators," *Smart Materials and Structures*, 13:N43–N50.

Zienkiewicz, O.C. and Taylor, R.L. 2000. *The Finite Element Method*. Solid Mechanics, Vol. 2, 5th edn, Butterworth-Heinemann, Oxford.

Zouari, W., Zineb, T.B. and Benjeddou, A. 2009. "A FSDT MITC Piezoelectric Shell Finite Element with Ferroelectric Non-linearity," *Journal of Intelligent Material Systems and Structures*, 20:2055–2075.

# APPENDIX

## Constitutive Relation

The elastic, piezoelectric and dielectric matrices of an orthotropic material polarized along the thickness direction 3 are detailed out in the following expression of the converse and direct piezoelectric effect:

$$
\begin{bmatrix} \sigma_{11} \\ \sigma_{22} \\ \sigma_{33} \\ \sigma_{23} \\ \sigma_{13} \\ \sigma_{12} \end{bmatrix} =
\begin{bmatrix}
C_{11} & C_{12} & C_{13} & 0 & 0 & 0 \\
 & C_{22} & C_{23} & 0 & 0 & 0 \\
 & & C_{33} & 0 & 0 & 0 \\
 & & & C_{44} & 0 & 0 \\
 & sym & & & C_{55} & 0 \\
 & & & & & C_{66}
\end{bmatrix}
\begin{bmatrix} \varepsilon_{11} \\ \varepsilon_{22} \\ \varepsilon_{33} \\ 2\varepsilon_{23} \\ 2\varepsilon_{13} \\ 2\varepsilon_{12} \end{bmatrix}
$$

$$
-
\begin{bmatrix}
0 & 0 & e_{31} \\
0 & 0 & e_{32} \\
0 & 0 & e_{33} \\
0 & e_{24} & 0 \\
e_{15} & 0 & 0 \\
0 & 0 & 0
\end{bmatrix}
\begin{bmatrix} E_1 \\ E_2 \\ E_3 \end{bmatrix}
$$

$$
\begin{bmatrix} D_1 \\ D_2 \\ D_3 \end{bmatrix} =
\begin{bmatrix}
0 & 0 & 0 & 0 & e_{15} & 0 \\
0 & 0 & 0 & e_{24} & 0 & 0 \\
e_{31} & e_{32} & e_{33} & 0 & 0 & 0
\end{bmatrix}
\begin{bmatrix} \varepsilon_{11} \\ \varepsilon_{22} \\ \varepsilon_{33} \\ 2\varepsilon_{23} \\ 2\varepsilon_{13} \\ 2\varepsilon_{12} \end{bmatrix}
$$

$$
+
\begin{bmatrix}
\epsilon_{11} & 0 & 0 \\
0 & \epsilon_{22} & 0 \\
0 & 0 & \epsilon_{33}
\end{bmatrix}
\begin{bmatrix} E_1 \\ E_2 \\ E_3 \end{bmatrix}
$$